

Spectral characteristics of propylitic alteration minerals as a vectoring tool for porphyry copper deposits



Luke C. Neal^a, Jamie J. Wilkinson^{a,b,c,*}, Philippa J. Mason^{a,b}, Zhaoshan Chang^{c,d}

^a Department of Earth Science and Engineering, Imperial College London, Exhibition Road, London SW7 2AZ, United Kingdom

^b LODE, Department of Earth Sciences, Natural History Museum, London SW7 5BD, United Kingdom

^c ARC Centre of Excellence in Ore Deposits (CODES), School of Geological Sciences, University of Tasmania, Hobart, Tasmania 7001, Australia

^d Economic Geology Research Centre (EGRU) and Academic Group of Geosciences, College of Science and Engineering, James Cook University, Townsville, Queensland 4011, Australia

ABSTRACT

Short-wave infrared (SWIR) reflectance spectroscopy is a quick and effective method of detecting and characterising hydrothermal alteration associated with ore deposits, and can identify not only mineral species but also changes in the major element composition of minerals. Porphyry deposits represent large accumulations of valuable metal in the Earth's crust and have extensive alteration signatures making them an attractive target for exploration, particularly by remote sensing which can cover large areas quickly. Reflectance spectroscopy has been widely applied in sericitic (phyllitic), argillic and advanced argillic alteration domains because it is particularly effective in discriminating bright clay minerals. However, the propylitic domain has remained relatively unexplored because propylitic rocks are typically dark and produce relatively poorly-defined spectra.

This study utilised an ASD TerraSpec 4 handheld spectrometer to collect SWIR spectra from rocks surrounding the Batu Hijau Cu-Au porphyry deposit in Indonesia, where previous work has identified systematic spatial variations in the chemistry of chlorite, a common propylitic alteration mineral. Spectra were collected from 90 samples and processed using *The Spectral Geologist* (TSG) software as well as the *Halo* mineral identifier to characterise mineralogy and extract the positions and depths of spectral absorption features, which were then correlated with major element geochemistry. Two diagnostic chlorite absorption features located at around 2250 nm and 2340 nm correlate with the Mg# ($\text{Mg}/[\text{Mg} + \text{Fe}]$) of chlorite, both in terms of wavelength position and depth. As the Mg# increases, the wavelengths of both features increase from 2249 nm to 2254 nm and from 2332 nm to 2343 nm respectively, and absorption depths also increase significantly. In the spatial dimension, these feature variations act as reasonably strong vectors to the orebody, showing systematic increases over a transect away from the porphyry centre, peaking at distances of around 1.6 km, which matches the spatial trend displayed by Mg#, as well as various trace element indicators in chlorite. The hull slope in spectra between 1400 nm and 1900 nm is also shown to increase with Mg#, and the position of an absorption feature at 1400 nm increases with the Al:Si ratio, a parameter that also tends to increase with proximity to porphyry deposits.

Feature depth variations in particular appear to represent a new finding in chlorite reflectance spectroscopy; however, the causes are not entirely clear and require further investigation. Nonetheless, the systematic behaviour provides a potentially useful new tool for exploration in propylitic alteration zones.

1. Introduction

Porphyry deposits represent some of the largest accumulations of metal in the Earth's crust and are the primary source of the world's Cu and Mo, and an important source of Au and other metals (Sillitoe, 2010). Deposits are formed as a result of hydrothermal fluids that exsolve from intrusive magmatic bodies, precipitating metals into the surrounding rocks. The outward movement of these hydrothermal

fluids creates distinct alteration zones recognised by the occurrence of specific mineral assemblages (Sillitoe, 2010; Cooke et al., 2014a). The propylitic alteration zone represents the most distal signature of mineralisation, detectable kilometres away from the main orebody (Cooke et al., 2014a) and, as such, is an important target for exploration. Alteration zoning is not only expressed in mineralogy, but in whole-rock and mineral geochemical trends which can act as vectors towards orebodies (e.g. Emmons, 1927; John, 1978; Norman et al., 1991; Cooke

* Corresponding author at: Department of Earth Science and Engineering, Imperial College London, Exhibition Road, London SW7 2AZ, United Kingdom.
E-mail address: j.wilkinson@nhm.ac.uk (J.J. Wilkinson).

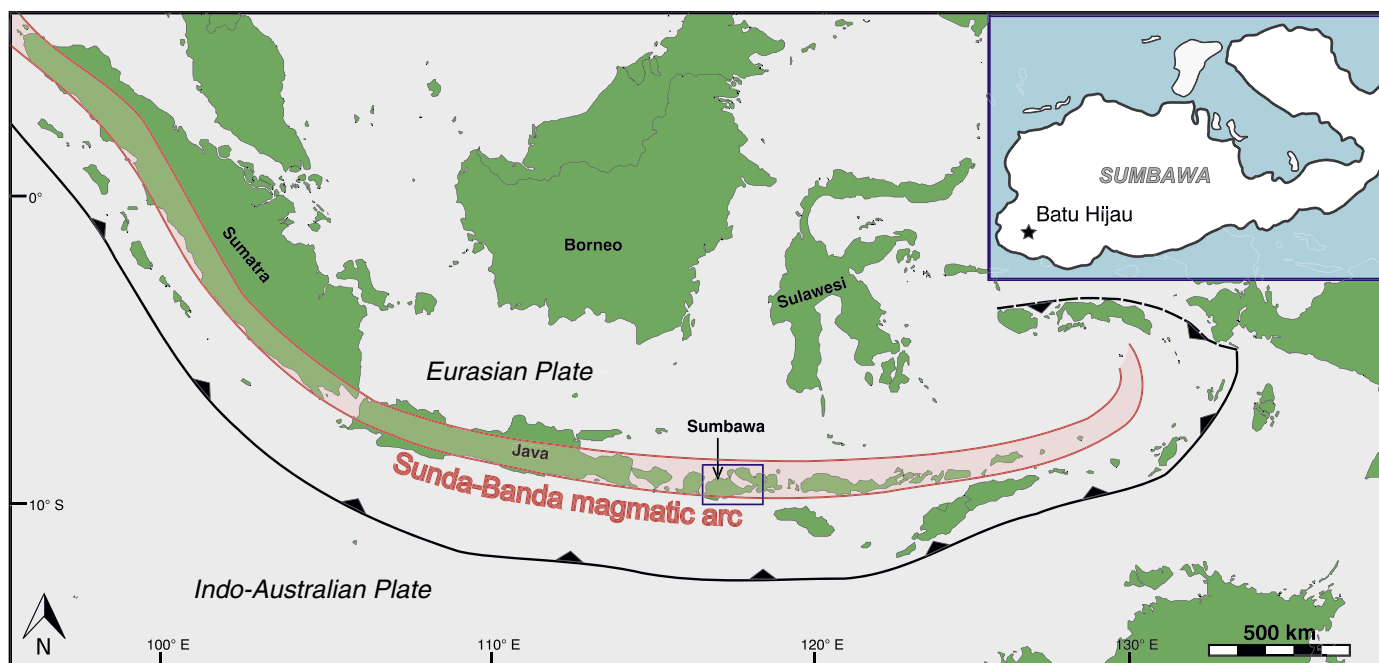


Fig. 1. Principal tectono-magmatic features of Indonesia. The major subduction zone is shown as well as the Sunda-Banda magmatic arc. Subduction of the Indo-Australian plate beneath the Eurasian plate produces the calc-alkaline magmatism that characterises the Cenozoic Sunda-Banda arc. Batu Hijau is located on the island of Sumbawa in the south-west (inset map). Modified after Garwin et al. (2005).

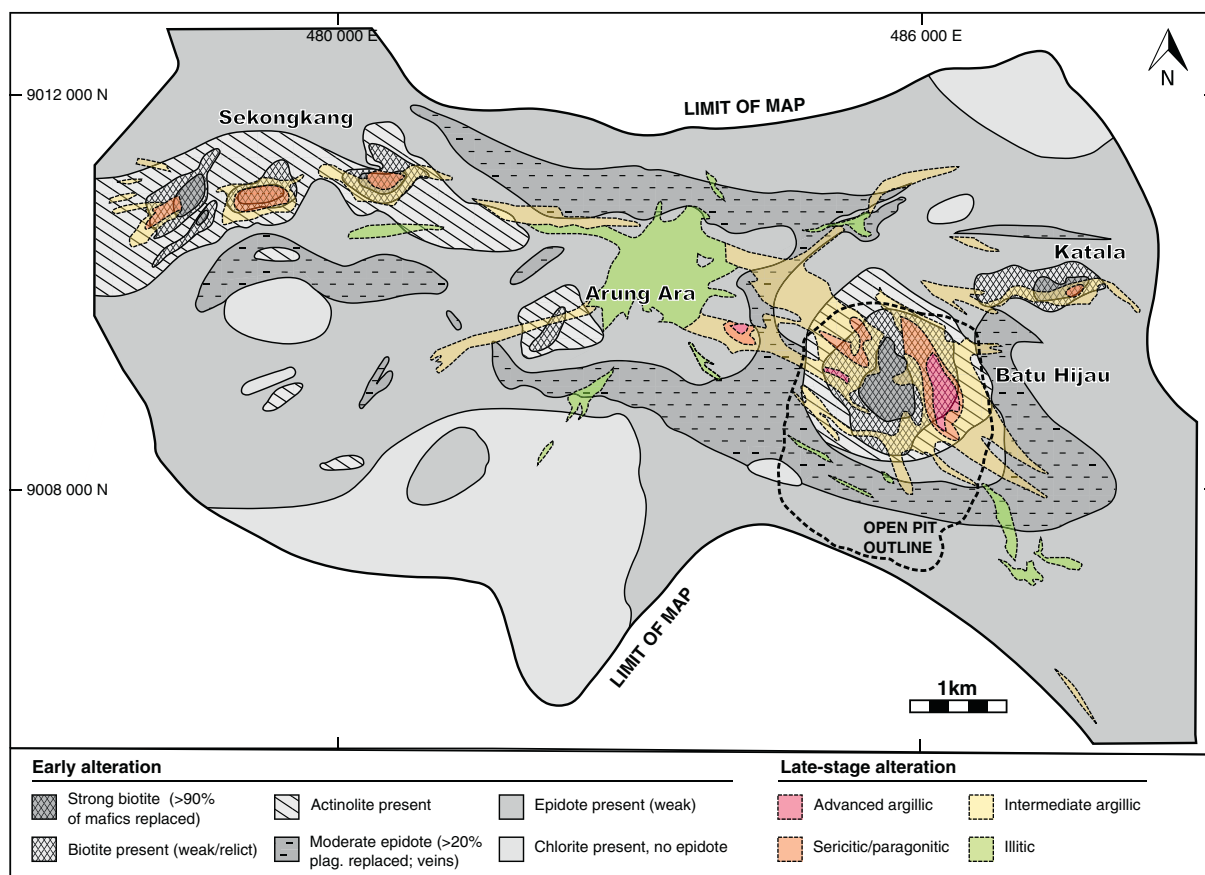


Fig. 2. Alteration map of the Batu Hijau district showing both early-stage (greyscale) and late-stage (colour) alteration. Modified after Garwin (2000). (For interpretation of the references to colour in this figure legend, the reader is referred to the web version of this article.)

Table 1

Technical specifications of the TerraSpec 4 spectrometer and Hi-Brite Contact Probe accessory that were used to collect infrared-spectra (ASD Inc., 2015).

ASD TerraSpec 4 Standard-Res Mineral Analyzer	
Wavelength range	350–2500 nm
VNIR detector	(350–1000 nm) 512 element silicon array
SWIR 1 & 2 detectors	(1001–1800 nm) & (1801–2500 nm) Graded Index InGaAs Photodiode, TE Cooled
Spectral resolution	3 nm (VNIR range)
(smallest detectable absorption feature)	10 nm (SWIR 1 & 2 range)
Wavelength accuracy	0.5 nm
Signal-to-noise ratio	9000:1 (VNIR & SWIR 1 range)
	4000:1 (SWIR 2 range)
Number of channels	2151
Acquisition software	Indico® Pro
Hi-Brite Contact Probe	
Light source	Halogen bulb, 2901 °K (± 10%)
Spot size	10 mm

et al., 2014b; Wilkinson et al., 2015).

Remote sensing is a valuable tool in mineral exploration, providing a quick way to identify and map hydrothermal alteration products over large areas. Much work has been done on characterising the hydrothermal alteration associated with ore deposits in terms of spectral signatures (Yang and Huntington, 1996; Herrmann et al., 2001; Sun et al., 2001; Jones et al., 2005) including porphyry deposits specifically (Cudahy et al., 2001; Chang et al., 2011; Dilles, 2012; Zadeh et al., 2014; Halley et al., 2015). However the focus of these studies is on the clay-dominated, argillic and sericitic alteration assemblages. In relation to a particular exploration application, Chang et al. (2011) showed that it is possible to use spectral features of alunite in the advanced-argillic alteration zone as pointers towards porphyry ore deposits.

Investigations into the SWIR spectroscopy of chlorite and epidote, two of the most prevalent propylitic alteration minerals, are few. However, sensitivity of SWIR spectra to mineral chemical changes that are recognisable both in the laboratory (King and Clark, 1989; Liebscher, 2004; Bishop et al., 2008) and in hyperspectral imaging (Cudahy et al., 2001; Roache et al., 2011) have been recognised. This indicates that spectral characteristics might be able to act as a vector to orebodies in the propylitic domain as well as the more proximal alteration zones.

The large footprint of propylitic alteration should present an attractive target for remotely sensed mineral exploration. However, the rocks that typify propylitic alteration zones are often dark (low reflectance) making their characterisation exceedingly difficult. Fortunately, the availability of increasingly sensitive portable field spectrometers has opened up the possibility of tackling this problem. These spectrometers are an ideal tool for detailed investigations into the spectral features of rocks; they can produce high-resolution spectra, free from the effects of atmospheric scattering and absorption, and have absorption features clearly detectable even at reflectance values as low as 1%.

This study utilised an ASD TerraSpec 4 spectrometer to collect infrared spectra of rocks from the Batu Hijau porphyry copper system in Indonesia. It builds on previous research done as part of the AMIRA P765A research project (AMIRA International Ltd., 2008) which included studies of spatial variation in the geochemistry of chlorite (Wilkinson et al., 2015) and epidote (Cooke et al., 2014b). Most importantly, the work utilised the same samples analysed by Wilkinson et al. (2015) so that extensive prior knowledge of whole-rock geochemistry and mineral chemistry was available. The primary aims were to characterise the infrared spectra of propylitic rocks throughout the

Batu Hijau alteration footprint, and to identify any spectral features that might reflect systematic geochemical variation in the spatial domain which could therefore act as vectors towards economic mineralisation. Longer term, it is hoped that such features could be targeted by airborne hyperspectral or even satellite remote sensors, such as ASTER or WorldView-3, allowing a relatively quick way to search large areas of propylitic alteration for contained porphyry deposits.

2. Background geology

Batu Hijau is a giant Cu-Au porphyry deposit located in the south-western part of Sumbawa island, Indonesia (Fig. 1). It is situated in the Sunda-Banda Arc which is host to numerous magmatic-hydrothermal deposits (Garwin et al., 2005), related to calc-alkaline magmatism resulting from subduction of the Indo-Australian Plate beneath the Eurasian plate. Prior to the start of open pit mining, Batu Hijau contained an estimated 1644 Mt of ore with copper and gold grades of 0.44% and 0.35 g/t respectively (Cooke et al., 2005).

The Batu Hijau district is largely made up of an Early to Middle Miocene volcanoclastic sequence which comprises volcanic lithic breccias and volcanic sandstones with local limestone layers. This is cut by several intrusive phases dating from the Early to Middle Miocene onwards which include andesites and andesite porphyries, quartz diorites, and porphyritic tonalites (Garwin, 2002). Mineralisation is strongly associated with tonalite porphyries in four main centres: Batu Hijau, Sekongkang, Arung Ara and Katala (Fig. 2). Batu Hijau is significantly larger and higher grade than the rest (Garwin, 2002). At least three intrusive episodes occurred in the Batu Hijau tonalite porphyry complex at the core of the system, with mineralisation and alteration intensity decreasing with each subsequent intrusion (Clode et al., 1999).

Potassic alteration, in the core of the Batu Hijau system, is typified by the replacement of hornblende groundmass in the host tonalites by biotite and magnetite. The surrounding propylitic alteration can be split into three subzones which, in order of increasing distance outwards, comprise: (1) actinolite ± epidote ± chlorite; (2) epidote + chlorite; and (3) chlorite (replacing mafic minerals) ± calcite ± albite (Fig. 2; Garwin, 2002; Clode et al., 1999). A transitional chlorite-sericite (intermediate argillic zone) developed after the propylitic and potassic alteration stages, overprinting the biotite (potassic) and actinolite zones (Idrus et al., 2009). Late-stage, structurally-controlled, argillic and advanced argillic alteration are widespread and overprint earlier alteration (Fig. 2; Clode et al., 1999; Garwin, 2002; Idrus et al., 2009).

3. Methodology

Short-wave infrared (SWIR) spectra were collected for 90 samples from the Batu Hijau deposit (Table 2). Samples were scanned in dark laboratory conditions using an ASD TerraSpec 4 reflectance spectrometer with the Hi-Brite Contact Probe accessory that acts as an illumination source and collects reflected light. Technical specifications are outlined in Table 1. Samples consisted of resin-mounted, polished rock slices, providing an ideal flat surface for the contact probe. Spectral files were created as an average of 3 scans at different points on each sample. Double the recommended scan time was used (10 s, following the recommendation of Chang and Yang, 2012 for dark, low reflectance rocks) to increase signal-to-noise ratios. Two sets of spectral files were generated via this process for each sample, acquired on different days, to assess the impact of differences in ambient lighting. In general, there is excellent agreement between the replicates (Table 2).

Spectra were primarily analysed using *The Spectral Geologist* (TSG) software, and selected for further investigation based on classification and mineral identification by *The Spectral Assistant* (TSA), a matching algorithm which identifies a linear mixture of two minerals in the library that best match the spectrum (CSIRO, 2010). Only spectra determined to contain either chlorite or epidote as the principal SWIR-active mineral phase (Table 2) were used in the subsequent analysis.

Table 2
Summary of sample data and principal minerals identified in SWIR spectra.

Sample ID	UTM Easting	UTM Northing	Lateral distance to centre (m)	Rock type	TSA primary mineral (A) ^b	TSA secondary mineral (A) ^b	TSA primary mineral (B) ^b	TSA secondary mineral (B) ^b	Halo primary mineral	Halo secondary mineral	Chlorite or epidote? ^c
B2-0.3 ^a	483270	9007990	2615	Andesite	Chlorite-FeMg	Epidote	Chlorite-FeMg	Epidote	FeMgChlorite	Mg-illite	Chlorite
B2-11.9 ^a	483279	9007982	2611	Andesite porphyry	Chlorite-FeMg	Epidote	Chlorite-FeMg	Epidote	Clinozoisite	Vermiculite	Chlorite
B2-23.0 ^a	483287	9007975	2607	Volcanic sandstone	Chlorite-FeMg	Epidote	Chlorite-FeMg	Epidote	FeMgChlorite	Mg-illite	Chlorite
B3-3.2 ^a	482933	9008262	2783	Volcanic sandstone	Chlorite-FeMg	NULL	Chlorite-FeMg	Kaolinite-PX	FeMgChlorite	Beidellite	Chlorite
BH-19	482597	9008864	2982	Andesite porphyry	Chlorite-FeMg	Epidote	Chlorite-FeMg	Epidote	FeMgChlorite	Corrensite	Chlorite
BH-20	483322	9009144	2297	Andesite porphyry	Chlorite-Mg	Epidote	Chlorite-FeMg	Epidote	FeMgChlorite	Epidote	Chlorite
BH-21	483645	9009000	1993	Volcanic breccia	Chlorite-FeMg	NULL	Chlorite-FeMg	Ankerite	FeMgChlorite	Vermiculite	Chlorite
BH-22	483738	9009248	1931	Andesite porphyry	Hornblende	Epidote	Hornblende	Epidote	Hornblende	Clinozoisite	Other/Null
BH-23	483817	9009356	1873	Volcanic breccia	NULL	NULL	NULL	NULL	Hornblende	Beidellite	Other/Null
BH-24	484282	9009242	1451	Volcanic breccia	NULL	NULL	NULL	NULL	FeMgChlorite	Mg-illite	Other/Null
BH-25	484605	9009320	1211	Volcanic breccia	Ankerite	Paragonite	Epidote	NULL	Vermiculite	Clinozoisite	Epidote
BH-57	483175	9008140	2626	Andesite porphyry	Epidote	Kaolinite-PX	Epidote	Kaolinite-PX	Epidote	KaolinitePX	Epidote
BH04-45	480050	9008240	2909	Andesite porphyry	Chlorite-Mg	Muscovite	Chlorite-Mg	Epidote	Chabazite	Clinozoisite	Epidote
BH04-52	484293	9008004	1924	Andesite porphyry	NULL	NULL	NULL	NULL	Vermiculite	Clinozoisite	Other/Null
BH04-53	484228	9007970	2000	Volcanic breccia	Chlorite-Mg	Epidote	Chlorite-Mg	Epidote	FeMgChlorite	Palygorskite	Chlorite
BH04-54	484207	9007930	2048	Volcanic breccia	Ankerite	Muscovite	Ankerite	Muscovite	Heulandite	Epidote	Other/Null
BH04-55B	484108	9007694	2293	Andesite porphyry	Aspectral	NULL	Aspectral	NULL	Phillipsite-Ca	Aragonite	Other/Null
BH05-70B ^d	480050	9008240	2909	Andesite porphyry	Chlorite-Mg	Epidote	Chlorite-Mg	Epidote	FeMgChlorite	Montmorillonite	Chlorite
BH05-71 ^d	479680	9008460	2608	Andesite porphyry	Chlorite-FeMg	Ankerite	Chlorite-FeMg	Epidote	Mg-illite	Mg-illite	Chlorite
BH05-72 ^d	479560	9008695	2356	Andesite porphyry	Muscovite	Epidote	Muscovite	Epidote	Vermiculite	Vermiculite	Other/Null
BH05-73 ^d	479425	9008955	2080	Volcanic breccia	NULL	NULL	NULL	NULL	Vermiculite	No match	Other/Null
BH05-74 ^d	479325	9009100	1928	Volcanic breccia	Ankerite	Kaolinite-PX	Siderite	Muscovite	Vermiculite	Clinozoisite	Other/Null
BH05-75 ^d	479230	9009290	1736	Andesite porphyry	Muscovite	Ankerite	Muscovite	Epidote	Heulandite	Epidote	Other/Null
BH05-76 ^d	479300	9009665	1367	Andesite porphyry	NULL	NULL	Chlorite-FeMg	Zoisite	FeMgChlorite	Iron Saponite	Chlorite
BH05-77 ^d	479335	9009830	1218	Andesite porphyry	NULL	NULL	NULL	NULL	Hornblende	Dolomite	Other/Null
BH05-78 ^d	479390	9010115	934	Andesite porphyry	Chlorite-FeMg	Paragonite	Chlorite-FeMg	Paragonite	FeMgChlorite	Rectortite	Chlorite
BH05-79 ^d	479395	9010215	834	Andesite porphyry	Chlorite-Mg	Epidote	Chlorite-Mg	Epidote	FeMgChlorite	Ammonio-Clay	Chlorite
BH05-80 ^d	479410	9010410	643	Andesite porphyry	Chlorite-Mg	Epidote	Chlorite-Mg	Epidote	FeMgChlorite	Ammonio-Clay	Chlorite
BH10-101	483820	9007524	2576	Volcanic breccia	Aspectral	NULL	Aspectral	NULL	Harmotome	Muscovite	Other/Null
BH10-102	483754	9007538	2610	Volcanic breccia	Aspectral	NULL	Aspectral	NULL	Phillipsite-Ca	FeMgChlorite	Other/Null
BH10-103	483644	9007490	2699	Andesite porphyry	NULL	NULL	NULL	NULL	Vermiculite	Clinozoisite	Other/Null
BH10-104	483374	9007308	2972	Andesite porphyry	NULL	NULL	NULL	NULL	Heulandite	Aragonite	Other/Null
BH10-105	483232	9007131	3173	Volcanic breccia	Aspectral	NULL	Aspectral	NULL	Heulandite	Epidote	Other/Null
BH10-106	483163	9006886	3380	Volcanic breccia	Aspectral	NULL	Aspectral	NULL	Heulandite	Aspectral	Other/Null
BH10-107	483009	9006784	3535	Volcanic breccia	Paragonite	Ankerite	Paragonite	NULL	Beidellite	Mg-illite	Other/Null
BH10-108	482891	9006649	3704	Volcanic breccia	Aspectral	NULL	Aspectral	NULL	Phillipsite-Ca	Aragonite	Other/Null

(continued on next page)

Table 2 (continued)

Sample ID	UTM Easting	UTM Northing	Lateral distance to centre (m)	Rock type	TSA primary mineral (A) ^b	TSA secondary mineral (A) ^b	TSA primary mineral (B) ^b	TSA secondary mineral (B) ^b	Halo primary mineral	Halo secondary mineral	Chlorite or epidote? ^c
BH10-109	482753	9006444	3930	Volcanic lithic breccia	NULL	NULL	Aspectral	NULL	Laumontite	Vermiculite	Other/Null
BH10-110	482604	9006283	4130	Volcanic lithic breccia	Aspectral	NULL	Aspectral	NULL	Heulandite	Vermiculite	Other/Null
BH10-111	482477	9006087	4344	Andesite porphyry	NULL	NULL	Aspectral	NULL	Phillipsite-Ca Hematite	Aspectral	Other/Null
BH10-112	482381	9005936	4510	Andesite porphyry	Aspectral	NULL	Aspectral	NULL	Phillipsite-Ca Hematite	Phillipsite-Ca Hematite	Other/Null
BH10-113	482355	9005921	4536	Volcanic lithic breccia	Siderite	Zoisite	Siderite	Zoisite	Vermiculite	Montmorillonite	Other/Null
BH10-114	482191	9005855	4692	Volcanic lithic breccia	NULL	NULL	NULL	NULL	Laumontite	Aspectral	Other/Null
BH10-115	481993	9005778	4875	Andesite porphyry	NULL	NULL	NULL	NULL	Aspectral	Other/Null	Other/Null
Ep-01	485539	9007759	1425	Volcanic lithic breccia	Epidote	Prehnite	Epidote	Prehnite	Epidote	Biotite	Epidote
Ep-02	485914	9007647	1579	Volcanic lithic breccia	Chlorite-FeMg	Paragoniticillite	Chlorite-FeMg	Paragoniticillite	FeMgChlorite	Rectorite	Chlorite
Ep-03	485900	9007545	1663	Andesite porphyry	Chlorite-FeMg	Muscovite	Chlorite-FeMg	Muscovite	Stilpnomelane	Clinozoisite	Chlorite
Ep-04	485898	9007438	1757	Andesite	Aspectral	NULL	Aspectral	NULL	Phillipsite-Ca	Clinozoisite	Other/Null
Ep-05	485883	9007322	1858	Volcanic lithic breccia	Chlorite-FeMg	Paragonite	Chlorite-FeMg	Paragonite	Stilpnomelane	Clinozoisite	Chlorite
Ep-06	486130	9007086	2133	Volcanic lithic breccia	Epidote	NULL	Epidote	NULL	Epidote	Palygorskite	Epidote
Ep-07	485919	9006964	2311	Volcanic lithic breccia	NULL	NULL	Aspectral	NULL	Phillipsite-Ca	Epidote	Other/Null
Ep-08	485751	9006859	2266	Andesite porphyry	NULL	NULL	NULL	NULL	Stilpnomelane	FeMgChlorite	Other/Null
Ep-09	485011	9011502	2644	Diorite	Chlorite-FeMg	Paragonite	Epidote	Paragonite	Stilpnomelane	Epidote	Chlorite/Ep Other/Null
Ep-10	485007	9011760	2890	Volcanic lithic breccia	NULL	NULL	NULL	NULL	Heulandite	Epidote	Other/Null
Ep-11	484951	9012003	3132	Volcanic lithic breccia	Aspectral	NULL	Aspectral	NULL	Phillipsite-Ca	Epidote	Other/Null
Ep-12	485333	9009875	1133	Andesite porphyry	Chlorite-FeMg	Paragonite	Chlorite-FeMg	Paragonite	Rectorite	FeMgChlorite	Chlorite
Ep-18	485875	9008347	1028	Andesite porphyry	NULL	NULL	NULL	NULL	Vermiculite	Ep Other/Null	Other/Null
SBD018-496.6	485615	9009036	450	Tonalite	Chlorite-Mg	Paragoniticillite	Chlorite-Mg	Paragoniticillite	Montmorillonite	Epidote	Chlorite
SBD018-619	485615	9009112	373	Tonalite	Chlorite-Mg	Paragoniticillite	Epidote	NULL	Stilpnomelane	FeMgChlorite	Chlorite/Ep Other/Null
SBD021-522.8	485633	9009146	465	Tonalite	Phengiticillite	Chlorite-FeMg	Chlorite-FeMg	Paragoniticillite	Mg-illite	FeMgChlorite	Chlorite
SBD130-21	484960	9008600	1134	Volcanic lithic breccia	NULL	NULL	NULL	NULL	Corrensite	FeMgChlorite	Other/Null
SBD143-41	484715	9008462	1331	Volcanic lithic breccia	Epidote	Paragonite	Chlorite-FeMg	Epidote	Epidote	Beidellite	Chlorite/Ep Other/Null
SBD143-49	484715	9008462	1326	Volcanic lithic breccia	Chlorite-FeMg	Paragonite	Epidote	Paragonite	FeMgChlorite	Rectorite	Chlorite/Ep Other/Null
SBD145-33	484841	9008488	1243	Volcanic lithic breccia	Epidote	NULL	Chlorite-FeMg	Epidote	Stilpnomelane	Epidote	Chlorite/Ep Other/Null
SBD145-73.2	484841	9008488	1214	Volcanic lithic breccia	Chlorite-FeMg	Epidote	Chlorite-FeMg	Epidote	Epidote	FeMgChlorite	Chlorite
SBD145-83	484841	9008488	1206	Volcanic lithic breccia	Epidote	NULL	Epidote	Calcite	Epidote	Clinozoisite	Epidote
SBD256-813	485607	9009204	236	Tonalite	Chlorite-Mg	Epidote	Chlorite-Mg	Epidote	Stilpnomelane	FeMgChlorite	Chlorite
SBD257-0965.6	485633	9008893	208	Tonalite	Chlorite-FeMg	Paragonite	Chlorite-Mg	Chlorite-FeMg	Stilpnomelane	Reactorite	Chlorite

(continued on next page)

Table 2 (continued)

Sample ID	UTM Easting	UTM Northing	Lateral distance to centre (m)	Rock type	TSA primary mineral (A) ^b	TSA secondary mineral (A) ^b	TSA primary mineral (B) ^b	TSA secondary mineral (B) ^b	Halo primary mineral	Halo secondary mineral	Chlorite or epidote? ^c
SBD276-876.4	485628	9009275	305	Carbonate	Kaolinite-PX	Paragonite	Kaolinite-PX	NULL	Jarosite	Phillipsite-Ca	Other/Null
SBD276-912.6	485629	9009258	296	Ash Tuff	Epidote	Kaolinite-PX	Montmorillonite	Epidote	Stilpnomelane	Epidote	Epidote
SBD284-100	484945	9008575	1080	Andesite porphyry	Chlorite-Mg	Epidote	Chlorite-Mg	Epidote	FeMgChlorite	Palygorskite	Chlorite
SBD284-1145	485415	9008924	120	Tonalite	Chlorite-Mg	Phlogopite	Chlorite-Mg	Paragoniticillite	Vermiculite	Mg-illite	Chlorite
SBD284-17.5	484911	9008549	1161	Volcanic lithic breccia	Epidote	NULL	Phlogopite	Epidote	Epidote	Montmorillonite	Chlorite/Epidote
SBD284-170	484973	9008596	1011	Andesite porphyry	Chlorite-Mg	Epidote	Chlorite-FeMg	Epidote	FeMgChlorite	Montmorillonite	Chlorite
SBD284-175.8	484975	9008598	1006	Andesite porphyry	NULL	NULL	Chlorite-Mg	Epidote	Vermiculite	Clinozoisite	Other/Null
SBD284-20	484912	9008549	1160	Volcanic lithic breccia	Epidote	NULL	NULL	NULL	Vermiculite	Clinozoisite	Epidote
SBD284-226	484995	9008614	957	Volcanic lithic breccia	NULL	NULL	Epidote	NULL	Vermiculite	Aragonite	Other/Null
SBD284-233	484998	9008616	950	Volcanic lithic breccia	Epidote	NULL	NULL	NULL	Epidote	Palygorskite	Epidote
SBD284-266	485011	9008626	917	Volcanic lithic breccia	NULL	NULL	Epidote	NULL	Epidote	Palygorskite	Other/Null
SBD284-306	485027	9008638	879	Volcanic lithic breccia	Hornblende	Ankerite	NULL	NULL	Vermiculite	Brucite	Other/Null
SBD284-375	485054	9008659	811	Volcanic lithic breccia	Chlorite-FeMg	Paragoniticillite	NULL	NULL	Beidellite	FeMgChlorite	Chlorite
SBD284-424	485073	9008675	764	Volcanic lithic breccia	Chlorite-Mg	Muscovite	NULL	NULL	Vermiculite	Clinozoisite	Chlorite
SBD284-775	485227	9008792	425	Andesite porphyry	NULL	NULL	Chlorite-Mg	Muscovite	Phillipsite-Ca	Reactorite	Other/Null
SBD284-95	484943	9008573	1085	Carbonate	NULL	NULL	NULL	NULL	Vermiculite	Aspectral	Other/Null
SBD284-965.5	485323	9008860	247	Carbonate	NULL	NULL	Ankerite	Paragonite	Phillipsite-Ca	Paragonite	Other/Null
SBD284-97	484943	9008574	1083	Andesite porphyry	Paragonite	Zoisite	NULL	NULL	Clinoptilolite	Muscovite	Other/Null
SBD284-1124	485404	9008916			Chlorite-FeMg	Paragoniticillite	NULL	NULL	Stilpnomelane	Vermiculite	Chlorite
SBD284-840	485260	9008815	363	Volcanic lithic breccia	Chlorite-FeMg	Paragoniticillite	NULL	NULL	Stilpnomelane	FeMgChlorite	Chlorite
SBD284-965.6	485323	9008860			Hornblende	Paragonite	NULL	NULL	Vermiculite	Ammonio-Clay	Other/Null
SBD299-0772.5	485540	9009360	404	Carbonate	Epidote	NULL	Epidote	NULL	Epidote	Palygorskite	Epidote
SBD304-619.6	485621	9008676	374	Ash Tuff	Aspectral	NULL	Aspectral	NULL	Phillipsite-Ca	Hornblende	Other/Null

Sample data and classification of mineralogy determined from the spectra. Radial distances to the nearest major porphyry centre are given for each sample; this is to Batu Hijau for most of the samples, but to the Sekonggang system for samples in the western traverse.

^a Samples collected from close to the Bumbu epithermal vein system.

^b (A) and (B) refer to the two separate sets of spectra acquired for each sample.

^c Principal mineral identified in spectra. "Chlorite/Epidote" refers to samples determined to be chlorite in one set of spectra and epidote in the other. It is probable that they contain roughly equal amounts of each.

^d Samples proximal to the Sekonggang porphyry centre (distances measured away from this).

Table 3
Summary of extracted spectral and compositional data.

Sample ID	2250 nm λ position	2340 nm λ position	1400 nm λ position	2250 nm depth	2340 nm depth	1400 nm depth	Hull slope index ^c	Data type	Chlorite data (EMP or LA-ICP-MS)							Epidote (EMP)			Whole rock Mg#
									Fe	Mg	Al	Si	Ca	Mg#	Al/(Al + Si)	Al	Fe		
B2-0.3 ^a	2253.2	2339.7	1404.6	0.307	0.423	0.187	1.59	LA ^b	16.71	14.59	10.88		0.136	0.466				0.37	
B2-11.9 ^b	2254.2	2340.0	1407.2	0.357	0.501	0.085	1.36	LA	15.46	10.51	10.00		0.124	0.405				0.29	
B2-23.0 ^a	2254.2	2340.8	1407.3	0.178	0.298	0.132	1.59	LA	15.92	10.25	10.00		0.171	0.392				0.28	
B3-3.2 ^a	2254.4	2342.1	1406.6	0.256	0.313	0.347	2.04	LA	15.09	9.95	10.00		0.117	0.397				0.26	
BH-19	2253.1	2338.9	1404.6	0.187	0.279	0.231	1.21	LA ^b	15.68	14.59	10.69		0.146	0.482				0.31	
BH-20	2253.4	2338.8	1402.4	0.134	0.282	0.127	1.34											0.32	
BH-21	2252.0	2338.0	1400.8	0.414	0.502	0.398	1.96	LA ^b	15.16	16.09	10.68		0.043	0.515				0.43	
BH-22	2252.4	2330.5	1402.6	0.067	0.169	0.071	1.21	LA	15.59	16.06	10.04		0.026	0.507				0.33	
BH-23	2250.2		1398.8		0.070	0.039	1.10											0.33	
BH-24	2252.1	2335.6	1400.7	0.121	0.200	0.124	1.30	EMP	13.88	12.44	10.06	13.40	0.097	0.473	0.429			0.30	
BH-25	2251.0	2339.0	1408.2	0.055	0.074	0.044	1.14	EMP	12.41	13.28	11.19	12.76	0.100	0.517	0.467			0.26	
BH-57	2254.4	2339.7	1413.0	0.070	0.203	0.051	1.07												
BH04-45	2252.8	2338.7		0.076	0.118		1.21	LA	14.02	14.91	8.90		0.327	0.515				0.03	
BH04-52	2248.4	2328.0	1401.9	0.025	0.037	0.027	1.05	EMP	13.41	12.30	8.83	14.31	0.229	0.478	0.382			0.29	
BH04-53	2252.7	2341.3	1408.0	0.093	0.183	0.035	1.24	EMP	13.47	11.97	9.83	14.03	0.311	0.470	0.412			0.23	
BH04-54	2252.1	2341.6	1414.7	0.028	0.078	0.054	1.16	EMP	12.86	10.86	10.49	14.89	0.364	0.458	0.413			0.30	
BH04-55B	2249.7	2342.6		0.011	0.009	0.046	1.07	EMP	12.13	11.63	9.31	14.92	0.321	0.490	0.384			0.34	
BH05-70B	2252.0	2337.7	1400.1	0.093	0.139	0.085	1.18	EMP	13.31	12.86	9.52	13.81	0.283	0.491	0.408	11.76	10.54	0.27	
BH05-71	2252.5	2338.9	1404.4	0.086	0.127	0.075	1.14	EMP	11.35	14.11	10.06	13.65	0.034	0.554	0.424	11.93	10.11	0.27	
BH05-72	2252.5	2340.9	1410.2	0.040	0.097	0.069	1.16	EMP	16.21	10.82	10.46	12.73	0.056	0.400	0.451	11.17	11.57	0.24	
BH05-73	2251.6		1402.6	0.049	0.172	0.144	1.52	EMP	17.46	10.23	9.81	13.10	0.400	0.369	0.428	13.91	7.21	0.33	
BH05-74	2249.8	2336.3	1407.2	0.030	0.046	0.056	1.08	EMP	12.16	13.72	9.32	13.95	0.078	0.530	0.400	11.83	9.81	0.31	
BH05-75	2251.5	2342.1	1413.6	0.065	0.102	0.124	1.18	EMP	11.90	13.85	10.82	13.25	0.020	0.538	0.450			0.28	
BH05-76	2252.9	2339.5	1401.6	0.086	0.117	0.100	1.27	EMP	16.13	11.10	9.38	13.56	0.145	0.408	0.409	12.78	8.35	0.30	
BH05-77			1397.0	0.092	0.097	0.106	0.92	EMP	17.54	11.12	7.64	14.57	0.167	0.388	0.344			0.35	
BH05-78	2251.8	2339.6	1403.3	0.235	0.279	0.337	1.33	EMP	14.14	11.31	11.02	13.50	0.018	0.444	0.449			0.48	
BH05-79	2252.0	2336.9	1399.9	0.068	0.111	0.120	1.11	EMP	16.99	11.15	9.60	13.20	0.016	0.396	0.421	12.01	10.25	0.29	
BH05-80	2252.3	2332.3	1401.9	0.071	0.149	0.124	1.15	EMP	14.55	12.24	10.25	13.12	0.030	0.457	0.439	11.93	10.39	0.32	
BH10-101	2246.3	2338.9		0.013	0.009	0.062	1.06	EMP	12.54	13.28	10.01	13.70	0.082	0.514	0.422			0.31	
BH10-102	2249.8	2339.6		0.016	0.018	0.056	1.06	EMP	13.29	12.89	9.07	14.35	0.176	0.492	0.387			0.31	
BH10-103	2250.5	2327.0	1399.8	0.031	0.050	0.071	1.03	EMP	14.25	12.12	8.70	14.81	0.464	0.460	0.370			0.35	
BH10-104	2249.5	2338.5	1414.6		0.012	0.056	1.02	EMP	9.67	12.03	10.53	15.56	0.512	0.554	0.404	11.07	10.83	0.27	
BH10-105	2249.5	2334.8		0.016	0.022	0.060	1.08	EMP	11.80	12.64	9.47	15.20	0.316	0.517	0.384	11.90	10.19	0.32	
BH10-106	2249.0	2328.6		0.008	0.010	0.059	1.10	EMP	11.55	13.21	9.19	14.83	0.293	0.534	0.383	11.84	9.98	0.32	
BH10-107	2248.0	2340.4	1411.5		0.031	0.086	1.03	EMP	11.09	11.50	11.18	14.74	0.322	0.509	0.431			0.32	
BH10-108	2245.2	2326.2			0.012	0.089	1.06	EMP	11.16	12.38	9.38	15.65	0.498	0.526	0.375			0.24	
BH10-109	2246.2	2341.0		0.007	0.019		1.09	EMP	12.58	12.74	8.76	15.34	0.354	0.503	0.363			0.29	
BH10-110	2245.6			0.005	0.013		1.04	EMP	10.27	14.00	8.47	15.83	0.464	0.577	0.349			0.32	
BH10-111	2247.4	2327.3			0.018	0.077	1.07	EMP	7.81	12.36	8.57	17.33	1.085	0.613	0.331			0.30	
BH10-112	2248.4				0.009	0.112	1.02	LA	5.30	18.90	7.89	17.56	1.027	0.781	0.310			0.23	
BH10-113	2250.5		1415.0		0.066	0.067	1.15	EMP	10.51	12.72	8.09	15.83	0.759	0.548	0.338			0.29	
BH10-114	2243.2				0.013		1.01	EMP	10.05	12.58	8.21	16.02	0.711	0.556	0.339			0.35	
BH10-115	2251.3	2325.3		0.044	0.037	0.090	1.01	LA	17.27	9.18	6.09	17.04	1.153	0.347	0.263			0.25	
Ep-01	2252.4	2342.1	1409.4	0.180	0.434	0.040	1.13	EMP	14.88	11.61	10.36	12.70	0.073	0.438	0.449	13.22	8.19	0.27	
Ep-02	2254.4	2342.6	1406.7	0.183	0.309	0.361	1.47	EMP	17.54	9.60	10.61	13.07	0.116	0.354	0.448	11.71	10.95	0.29	
Ep-03	2252.9	2343.3	1410.3	0.112	0.163	0.296	1.52	EMP	16.93	10.21	10.47	13.10	0.116	0.376	0.444	13.08	8.71	0.30	
Ep-04	2248.9	2346.4	1414.3	0.026	0.070	0.121	1.13	EMP	18.43	9.32	9.64	13.48	0.194	0.336	0.417	11.51	10.73	0.24	
Ep-05	2252.7	2342.3	1406.6	0.119	0.167	0.256	1.65	EMP	15.43	10.83	10.43	13.37	0.129	0.412	0.438			0.33	
Ep-06	2252.8	2338.7	1411.0	0.122	0.329	0.035	1.20	EMP	13.09	11.85	10.57	13.23	0.141	0.475	0.444	13.19	8.22	0.30	
Ep-07	2250.6	2338.0	1413.3	0.040	0.066	0.105	1.22	EMP	12.92	12.28	10.01	13.83	0.152	0.487	0.420	12.16	9.41	0.33	
Ep-08	2251.7	2331.1	1400.9	0.051	0.066	0.093	1.11	EMP	15.89	11.85	8.52	13.77	0.189	0.427	0.382			0.35	

(continued on next page)

(continued on next page)

Table 3 (continued)

Sample ID	2250 nm λ	2340 nm λ	1400 nm λ	2250 nm depth	2340 nm depth	1400 nm depth	Hull slope index ^c	Data type	Chlorite data (EMP or LA-ICP-MS)							Epidote (EMP)		Whole rock Mg#
									Fe	Mg	Al	Si	Ca	Mg#	Al/(Al + Si)	Al	Fe	
Ep-09	2252.4	2339.6	1405.8	0.158	0.295	0.216	1.54	EMP	14.26	11.52	10.48	13.40	0.177	0.447	0.439	11.46	11.21	0.38
Ep-10	2251.2	2339.0	1416.9	0.024	0.038	0.129	1.08	EMP	11.69	10.97	10.98	14.41	0.372	0.484	0.432	11.41	10.70	0.33
Ep-11	2250.2	2339.9		0.018	0.020	0.067	1.04	EMP	12.32	12.53	10.00	13.82	0.163	0.504	0.420	12.03	9.87	0.27
Ep-12	2252.3	2341.2	1409.2	0.052	0.055	0.069	1.09	EMP	11.95	13.24	11.68	12.50	0.006	0.526	0.483			0.21
Ep-18	2251.5	2331.7	1415.5	0.024	0.058	0.051	1.06	EMP	10.29	14.23	10.50	13.34	0.108	0.580	0.440	12.52	9.19	0.33
SBD018-496.6	2248.6	2337.8	1409.6	0.045	0.056	0.119	1.05	EMP	13.00	12.83	10.42	13.21	0.074	0.497	0.441	11.78	10.42	0.20
SBD018-619	2251.8	2337.6	1409.6	0.070	0.105	0.095	1.10	EMP	11.61	13.83	9.66	13.68	0.084	0.544	0.414	12.54	9.11	0.20
SBD021-522.8	2249.0	2338.9	1410.3	0.044	0.081	0.141	1.15	EMP	14.42	11.84	10.83	12.75	0.040	0.451	0.459			0.17
SBD130-21	2249.4	2326.2	1396.4	0.064	0.107	0.070	1.09	EMP	11.37	13.99	10.57	13.23	0.048	0.552	0.444			0.29
SBD143-41	2254.2	2340.9	1408.8	0.185	0.343	0.065	1.19	EMP	14.16	9.97	11.55	13.42	0.185	0.413	0.463			0.29
SBD143-49	2254.4	2340.9	1408.3	0.175	0.278	0.137	1.39	EMP	16.47	9.53	12.02	12.48	0.074	0.367	0.491			0.31
SBD145-33	2252.8	2339.4	1409.7	0.163	0.295	0.182	1.28	EMP	14.04	11.67	10.92	13.18	0.086	0.454	0.453			0.29
SBD145-73.2	2253.2	2338.4	1402.8	0.339	0.540	0.127	1.58	EMP	15.00	11.94	10.80	12.80	0.046	0.443	0.458			0.28
SBD145-83	2253.7	2339.0	1410.0	0.274	0.521	0.033	1.21	EMP	15.21	11.04	11.66	12.21	0.074	0.420	0.489			0.28
SBD256-81.3	2250.9	2335.7	1403.3	0.071	0.115	0.134	1.18	EMP	11.14	13.36	9.71	13.59	0.134	0.545	0.417	12.17	9.76	0.26
SBD257-0965.6	2251.8	2338.8	1409.7	0.089	0.164	0.268	1.28	EMP	13.08	12.68	10.44	13.00	0.064	0.492	0.445	11.46	11.31	0.17
SBD276-876.4	2250.9	2332.3	1414.1		0.043	0.180	1.22									12.49	9.09	0.44
SBD276-912.6	2252.3	2336.8	1412.4	0.128	0.326	0.250	1.39									12.18	10.19	0.20
SBD284-100	2250.9	2338.3	1401.7	0.076	0.111	0.043	1.15	LA ^b	13.28	17.14	10.00		0.029	0.563				0.34
SBD284-1145	2249.6	2329.1	1404.5	0.034	0.085	0.110	1.42	EMP	14.34	11.88	10.48	12.96	0.097	0.453	0.447			0.17
SBD284-17.5	2253.0	2339.7	1408.8	0.115	0.220	0.113	1.25	EMP	15.01	11.75	10.82	12.60	0.034	0.439	0.462			0.28
SBD284-170	2250.3	2336.5	1402.9	0.077	0.100	0.042	1.17	EMP	11.12	14.42	10.59	13.23	0.027	0.565	0.444			0.31
SBD284-175.8	2248.1	2325.2	1400.2	0.029	0.049	0.040	1.07	EMP	10.78	14.56	10.67	13.35	0.086	0.574	0.444			0.31
SBD284-20	2252.2	2339.6	1408.6	0.104	0.164	0.108	1.31	EMP	14.46	12.27	10.96	12.73	0.029	0.459	0.463			0.26
SBD284-226	2250.2	2339.6	1396.0		0.052	0.046	1.04	EMP	10.21	14.63	10.70	13.76	0.127	0.589	0.437			0.31
SBD284-233	2253.2	2338.1		0.113	0.365	0.032	1.12	EMP	16.07	9.47	9.91	14.32	0.469	0.371	0.409			0.14
SBD284-266	2253.9	2339.7	1419.9	0.063	0.214	0.017	1.03	EMP	11.84	14.42	10.32	13.53	0.038	0.549	0.433			0.27
SBD284-306	2248.1		1399.0	0.010	0.028	0.028	1.02	EMP	10.90	14.45	10.59	13.45	0.040	0.570	0.440			0.29
SBD284-375	2251.3	2340.1	1412.5	0.041	0.062	0.090	1.05	EMP	11.84	13.03	11.57	13.15	0.028	0.524	0.468			
SBD284-424	2249.4	2334.1	1401.1	0.053	0.065	0.042	1.14	EMP	11.75	13.65	9.16	14.49	0.163	0.537	0.387			0.25
SBD284-775		2347.0	1417.4		0.014	0.165	1.45											0.18
SBD284-95	2250.0	2330.2	1402.8	0.055	0.070	0.074	1.20	EMP	11.61	13.90	10.88	12.84	0.034	0.545	0.459			0.33
SBD284-965.5	2251.7	2339.9	1413.9	0.025	0.051	0.074	1.23	EMP	12.16	12.98	10.85	13.10	0.075	0.516	0.453			0.25
SBD284-97	2249.9	2339.7	1413.7		0.038	0.108	1.18	EMP	11.94	13.60	10.88	12.96	0.039	0.532	0.456			0.25
SBD284-1124	2250.8	2333.9	1411.7	0.036	0.060	0.074	1.35											0.38
SBD284-840	2251.8	2336.5	1408.7	0.080	0.122	0.095	1.40											
SBD284-965.6	2253.0	2343.5	1412.2	0.071	0.071	0.157	1.23											
SBD299-0772.5	2252.8	2336.5	1414.1	0.143	0.417	0.120	1.32									11.22	11.55	0.13
SBD304-619.6	2251.1	2331.0		0.021	0.094	0.170	1.16	EMP	19.76	9.11	10.48	12.19	0.075	0.315	0.462	11.41	11.54	0.17

All geochemical data (except ratios) reported in weight percent, and averaged from multiple readings per sample. Outliers were removed prior to averaging (see text for details). Geochemical data are derived from the AMIRA P765A project database.

^a Samples collected from close to the Bambu epithermal vein system.

^b LA-ICP-MS data with anomalously elevated Fe and Mg values (not used in analysis).

^c 'Hull slope index' = reflectance at 1850 nm/reflectance at 1440 nm.

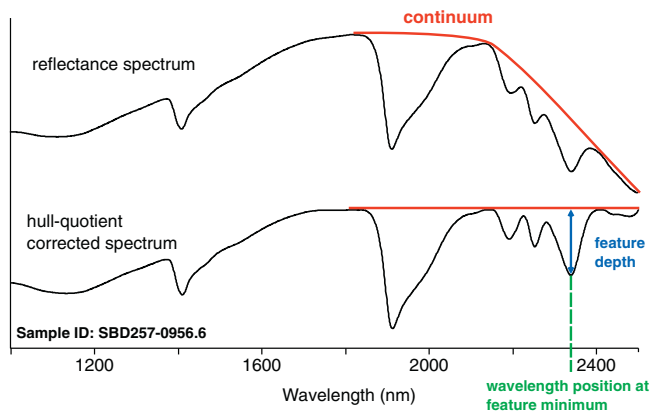


Fig. 3. A standard reflectance spectrum (top) compared to a spectrum with the hull-quotient correction applied (bottom) which removes the continuum caused by broader background variation. The feature depth and the wavelength position at minimum, two important spectral characteristics, are also illustrated for one absorption feature.

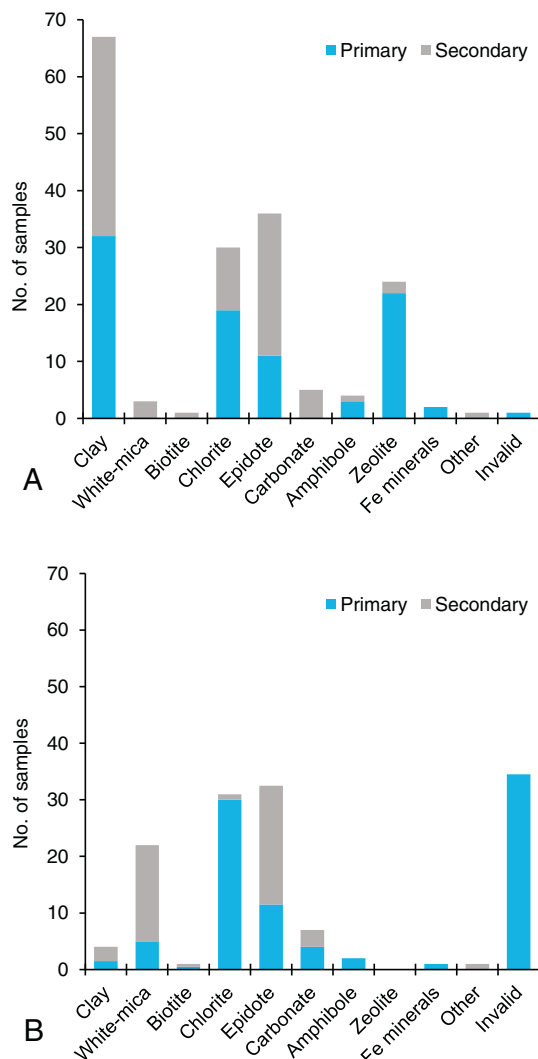


Fig. 4. Abundance of primary and secondary mineral groups as determined by: (A) *The Spectral Assistant* (TSA); and (B) the Halo mineral identifier. Invalid refers to samples where no mineral could be identified from the spectrum.

Wavelength positions and depths of features were calculated from the two average spectra for each individual sample. The average of these results are given in Table 3. These values were extracted from the

profiles of hull-quotient corrected spectra; this correction accentuates absorption features by removing broad background variation (Fig. 3).

Analysis of the spectra was also undertaken by ASD Inc. (PANalytical) utilising the Halo mineral identifier in order to compare results obtained using a different matching algorithm. The considerably larger library of mineral spectra that Halo incorporates also enabled the identification of additional minerals that TSG could not.

Geochemical data were previously collected as part of the AMIRA P765A project. These data include whole-rock geochemistry, electron microprobe analyses (EMP) of chlorite and epidote grains, and laser ablation inductively-coupled-plasma mass spectrometry (LA-ICP-MS) analyses of chlorite grains (Table 3). EMP data were primarily used to define the major element compositions of minerals; this was acquired on multiple spots on multiple grains in each sample, with an average of 10 measurements per sample. These were validated based on stoichiometry prior to inclusion in the database. Chlorite LA-ICP-MS data were used to define major element chemistry in four samples where EMP data were not available. Outliers in the EMP data were identified as any measurements where at least one major element (Fe, Al, Si, O, Mg, Ca) fell outside the bounds of the mean of the dataset $\pm 2\sigma$ for each mineral. Multiple spot analyses for each sample were averaged and $\pm 1\sigma$ standard error used as a practical measure of combined analytical uncertainty and natural, within-sample variability.

4. Results

4.1. Spectrally-determined mineralogy

The Spectral Assistant identified chlorite and epidote as the most abundant SWIR-active mineral groups in the samples, with white-mica and carbonates also making up significant contributions (Figs. 4A, 5A, B). Chlorite, where identified, was almost always the primary mineral. Epidote was common as the second most abundant SWIR-active mineral in chlorite-dominated mineral. The results from Halo (Figs. 4B, 5B) were generally similar, but identified clays (primarily smectites and vermiculites) as dominant in the biotite and actinolite zones, with chlorite commonly attributed as the secondary mineral. Although the identification of these phases should be treated with caution, their presence would be consistent with the later argillic overprint that has been well mapped in the proximal parts of the alteration system (Fig. 2). Halo also classified many spectra that TSA could not, with most being zeolite-dominant, particularly in the very distal samples. Minerals contained in each group are shown in Table 4.

Of the 90 samples, 46 produced spectra with the primary mineral identified by TSA as either chlorite or epidote (Fig. 5C). Of this subset, 30 were attributed to containing primarily chlorite, 10 to containing primarily epidote, and 6 where it was unclear (likely containing roughly equal amounts of each). Separate spectra collected on different areas of the same sample were very consistent (Fig. 6) indicating that the SWIR response is reproducible and varies more between samples (as a function of spatial position and mineral abundance) than within samples.

4.2. Chlorite

Chlorite chemistry from throughout the propylitic zones at Batu Hijau shows significant variation in terms of Fe and Mg which have a strong inverse correlation (Fig. 7A) related to the well-established solid solution between the iron and magnesium end-members (Deer et al., 2009). The Mg/(Mg + Fe) mass ratio (Mg#) ranges from 0.30 to 0.62 which translates to Mg/Fe molar ratios between 0.78 and 0.51 with a mean of 0.68 ± 0.01 (1σ). Comparison of chlorite Mg# to the whole-rock Mg# shows no correlation (Fig. 7B) suggesting a lack of protolith control of chlorite composition. Si content shows an inverse correlation with Al (Fig. 7C), probably as a result of the Tschermak substitution: $Al^{3+} + Al^{3+} = Si^{4+} + M^{2+}$ (Deer et al., 2009). Ca is also strongly

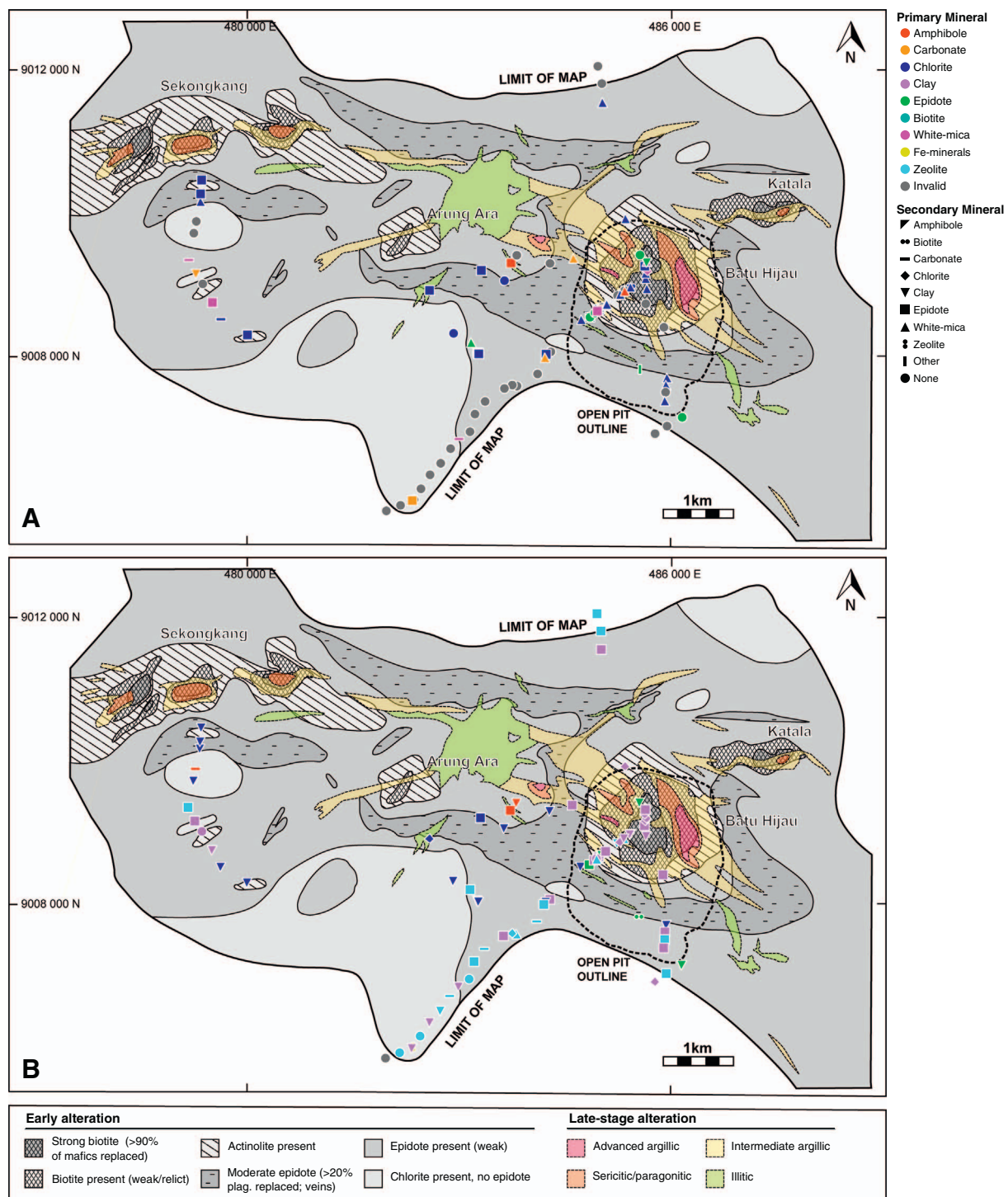


Fig. 5. Spectrally-determined mineralogy of the samples overlaid on alteration maps of Batu Hijau. Colour corresponds to the primary mineral group and shape corresponds to the secondary mineral group. (A) Classification of spectra by *The Spectral Assistant*. (B) Classification of spectra as determined by *The Halo* mineral identifier. (C) Samples classified according to their dominant mineral (from TSG). ‘Chlorite/Epidote’ refers to samples classified as chlorite in one instance, and epidote in the other – it is probable that they contain roughly equal amounts of each. Samples classified as ‘Other/Invalid’ were not used in any analysis involving spectral features. Base map modified after Garwin (2000).

correlated with Si and inversely correlated with Al (Fig. 7D).

Chlorite-dominated spectra are characterised by two key absorption features centred around 2250 nm and 2340 nm (Fig. 8), caused by Fe–OH and Mg–OH bond stretching respectively (Herrmann et al., 2001). A third feature occurs at around 2000 nm but this is masked by a large feature at 1910 nm, present in all samples, that is attributable to the presence of molecular water. A feature at around 1400 nm is also

consistently present, caused by OH^- (Clark et al., 1990; Bishop et al., 2008), but is not diagnostic of chlorite. In many samples, an absorption feature at around 2195 nm is probably a result of the presence of clay minerals containing Al–OH groups (Clark et al., 1990; Herrmann et al., 2001). There is also a notable slope (hull) that descends from ~1900 nm to ~1400 nm with variable gradient.

Within the spectra classified as chlorite-dominant, the most

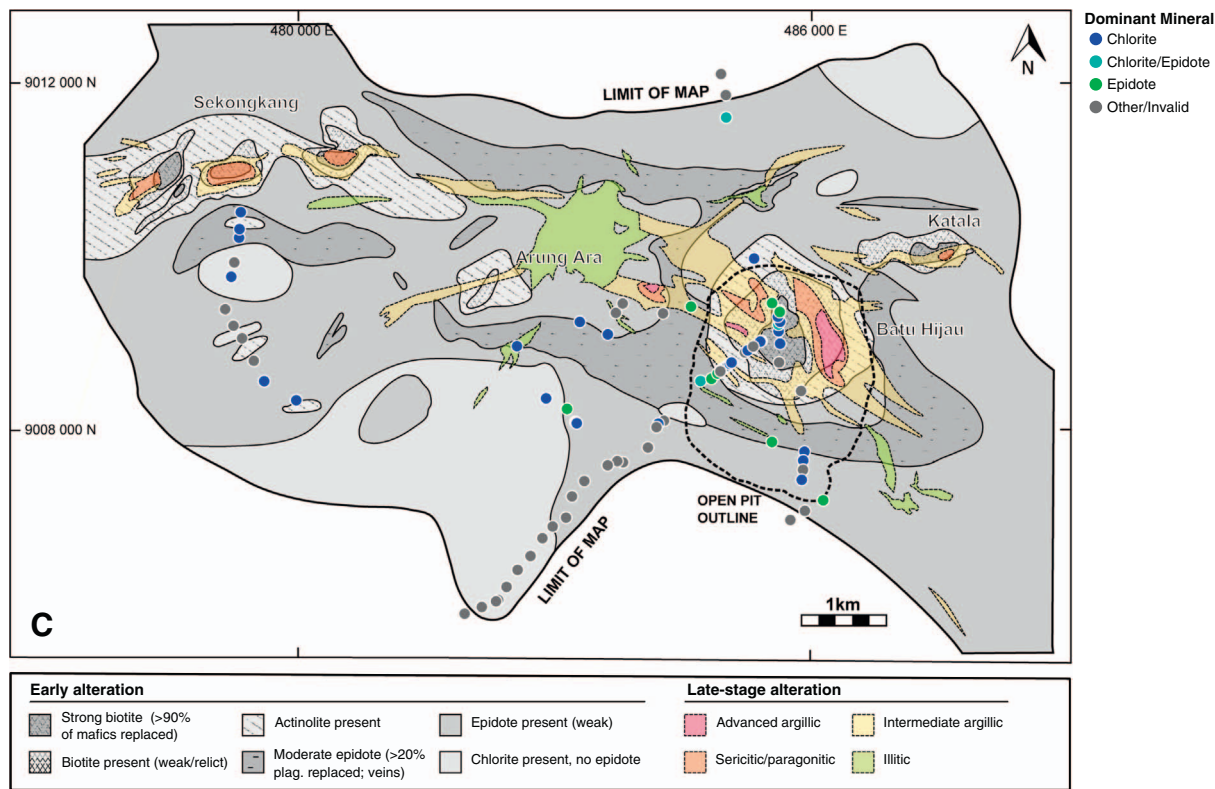


Fig. 5. (continued)

Table 4
Classification of minerals (as identified and named by TSG and Halo) into mineral groups used in Figs. 4, 5A, 5B.

Amphibole	Biotite	Carbonate	Chlorite	Clay	Epidote	Fe-minerals	White-mica	Zeolite	Other
Hornblende	Biotite Phlogopite	Calcite Aragonite Dolomite Ankerite Siderite	Chlorite Corrensite	Mg-illite Vermiculite Beidellite Palygorskite Kaolinite Montmorillonite Iron saponite Rectorite Ammonio-clay Stilpnomelane	Epidote Clinzoisite Zoisite	Hematite Jarosite	Muscovite Paragonite Paragonitic illite Phengitic illite	Chabazite Heulandite Phillipsite-Ca Harmotome Laumontite Clinoptilite	Brucite Prehnite

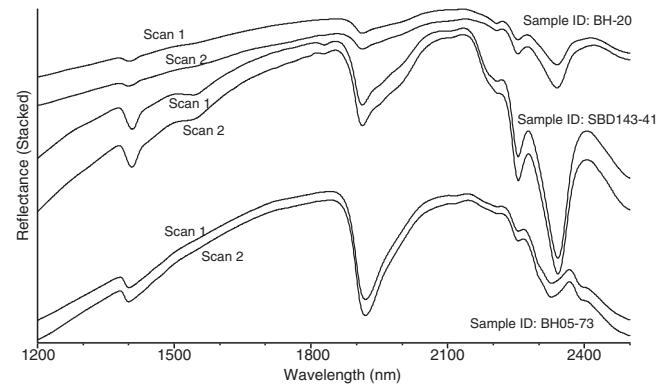


Fig. 6. Comparisons between two, separately obtained spectra taken for the same sample (shown in three examples). Spectra are very consistent despite being obtained separately on different days, at different points on each rock sample.

noticeable variation occurs in the position and depth of absorption features centred around 2250 nm and 2340 nm, which are strongly coupled (Fig. 9). For the absorption centred around 2250 nm, the exact wavelength position of the feature minimum varies between 2255 nm and 2248 nm. For the absorption centred around 2340 nm this varies between 2343 nm and 2328 nm. The maximum depth of both features varies between 0.03 and 0.55 (fraction of reflectance range).

The positions of these two features show a relatively strong inverse correlation with the Mg# of chlorite in the samples (Fig. 10). Samples containing more Mg-rich chlorite correspond to spectra where both the 2250 nm and 2340 nm features are shifted to lower wavelengths. Spectra with absorption feature minima at the lowest wavelengths appear to be anomalous, with wavelength values more in fitting with the samples not classified as chlorite-dominated.

The depth of both features also shows a negative correlation with the Mg#, which is considerably stronger at depths below ~0.34 (Fig. 11). Data points with greater depth values appear to be more in the range of depths shown by epidote-dominated samples.

Changes in the slope of the hull between 1900 nm and 1400 nm are

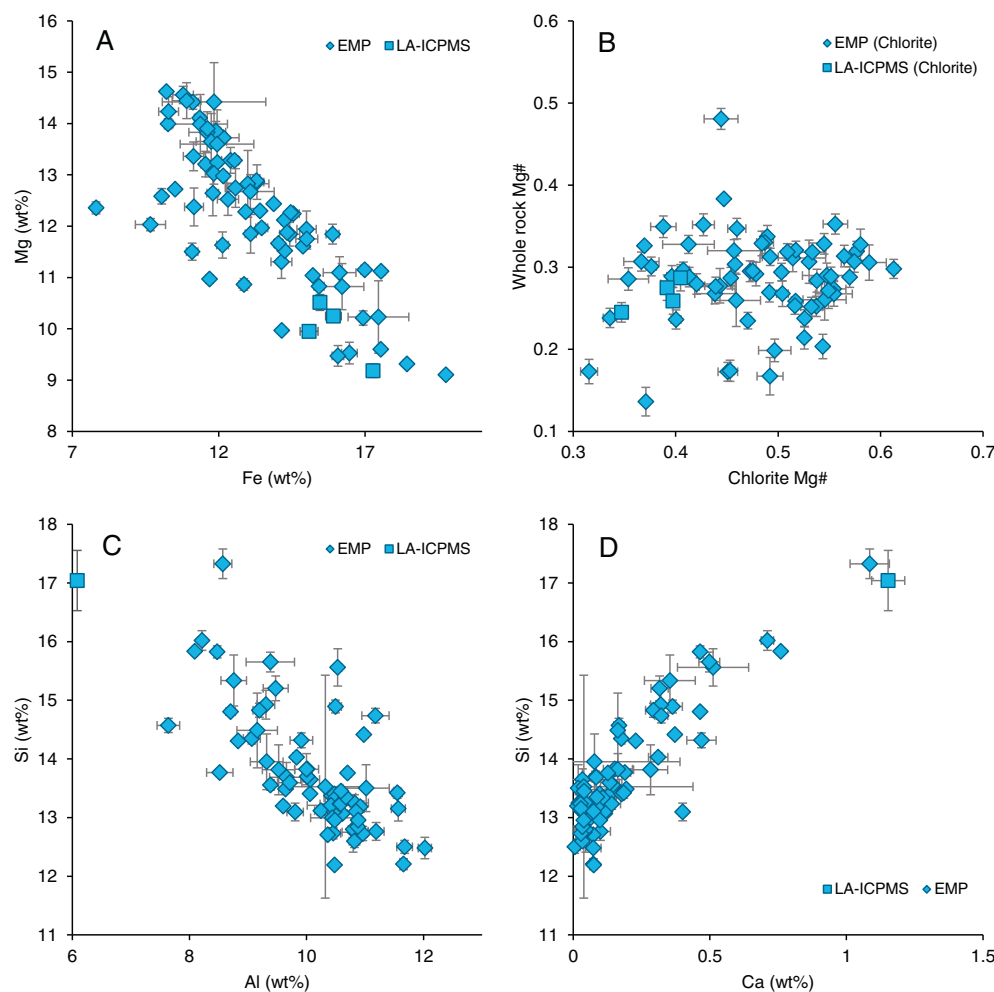


Fig. 7. Plots of element concentrations for chlorite grains. Data are averaged for each sample and 1σ standard error bars are shown. EMP and LA-ICPMS data are shown in different symbols. (A) Mg concentration plotted against Fe concentration showing a positive correlation. (B) Whole rock Mg# plotted against chlorite Mg# showing no correlation ($R^2 = 0.017$). Si concentration plotted against Al concentration for chlorite grains. A negative correlation is seen between Si and Al content. (D) Si concentration plotted against Ca concentration showing a positive correlation. Data derived from AMIRA P765A project database.

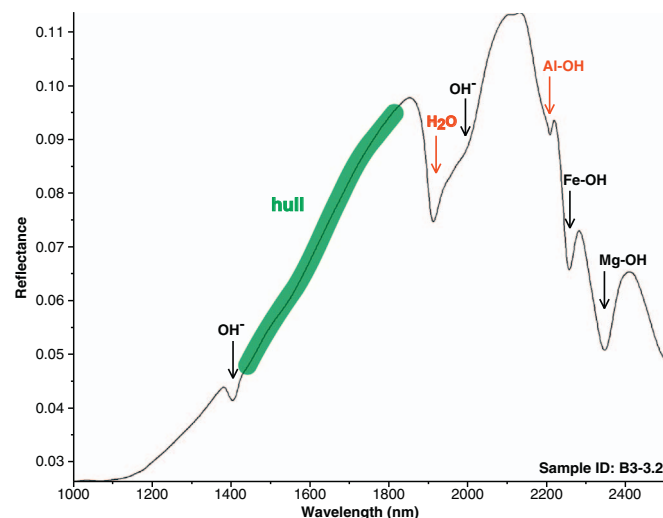


Fig. 8. SWIR spectrum of a sample predominantly made up of chlorite (according to *The Spectral Assistant*). Diagnostic features include the Fe-OH and Mg-OH absorption features at ~ 2250 and ~ 2340 nm, the weak (masked) feature at ~ 2000 nm and the hull between ~ 1900 nm and ~ 1400 nm. Red labels indicate features in the spectrum caused by the presence of other minerals. (For interpretation of the references to colour in this figure legend, the reader is referred to the web version of this article.)

also observed, with more Fe-rich samples having a steeper slope (Fig. 12). The aforementioned features are illustrated in selected spectra (Fig. 13).

The position of the OH^- absorption feature at around 1400 nm also shows systematic variation which correlates fairly strongly with the Al:Si ratio of chlorite in the samples, with Al-rich chlorite producing spectra with the feature shifted to higher wavelengths (Fig. 14).

4.3. Epidote

Epidote geochemistry shows most variation with respect to Fe and Al (Table 3) representing the solid solution between epidote and clinozoisite. Molar Fe:Al ratios range from 0.50 to 0.24 , meaning all samples (except one) fall into the classification of epidote (Franz and Liebscher, 2004). Other major elements, including Ca, show remarkably little variation.

In epidote-dominated spectra (Fig. 15) two absorptions are once again observed at around 2250 nm and 2340 nm, caused by Fe–OH bonds (Clark et al., 1990). However, the most diagnostic feature occurs at ~ 1550 nm and the presence of epidote in a sample is most readily identified by this. Once again, absorptions are seen at ~ 1400 nm and ~ 1910 nm.

The range in wavelength positions of the 2250 nm and 2340 nm absorption features (2251 – 2255 nm and 2336 – 2342 nm respectively) is significantly less than in chlorite. The depth of the 2340 nm feature is generally greater than in chlorite (mean = 0.3 compared with 0.2) but that of the 2250 nm absorption is about the same (Table 3). No significant variations in absorption features were observed that correlate with chemical composition (e.g. the Fe:Al ratio), however this may be due, in part, to a paucity of data.

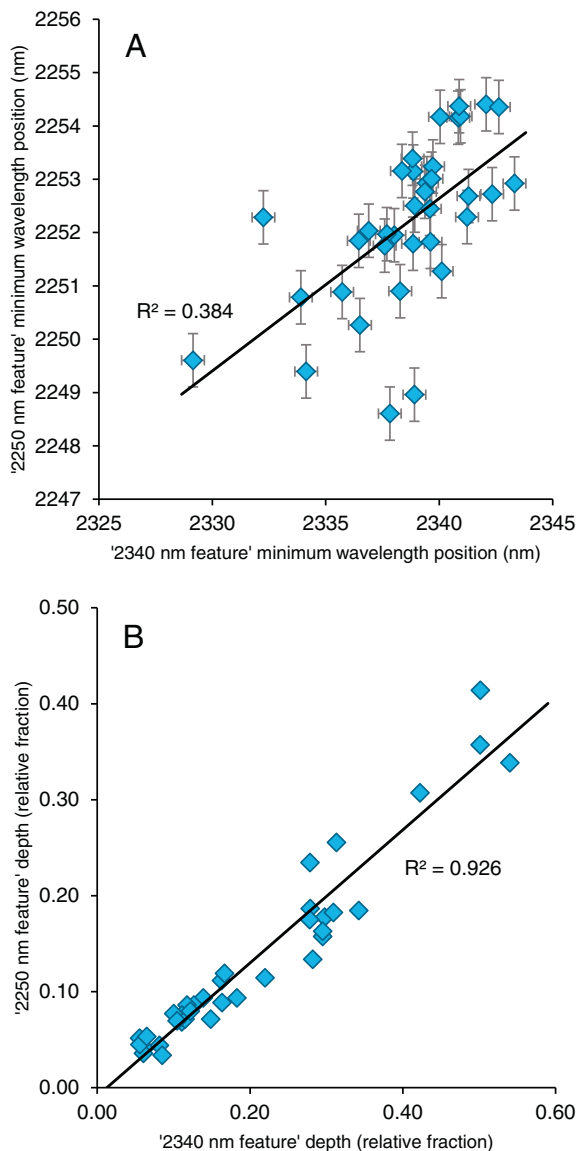


Fig. 9. Plots showing the coupling of absorption features at 2250 nm and 2340 nm. (A) Wavelength positions at absorption minima showing a positive correlation. (B) Relative absorption depths showing a positive correlation.

4.4. Spatial patterns in chlorite spectral response and chemistry

A number of spectral and chemical features of chlorite vary spatially, relating primarily to distance away from the Batu Hijau porphyry centre and from the Sekongkang prospect.

4.4.1. 2250 and 2340 absorption positions

The wavelength position of the features at 2250 nm and 2340 nm are lowest near the centre of the Batu Hijau system, and show a systematic shift to longer wavelengths away from the centre, providing a strong vector to the orebody (Fig. 16). Plotting the data as a function of radial distance from the centre reveals a general increase of the wavelength positions from the centre to ~1.2 km, beyond which the values generally plateau (Fig. 17), approximately coincident with the edge of the actinolite subzone. The 2340 nm feature also follows this trend in the northwest with respect to the Sekongkang porphyry centre (Fig. 16B).

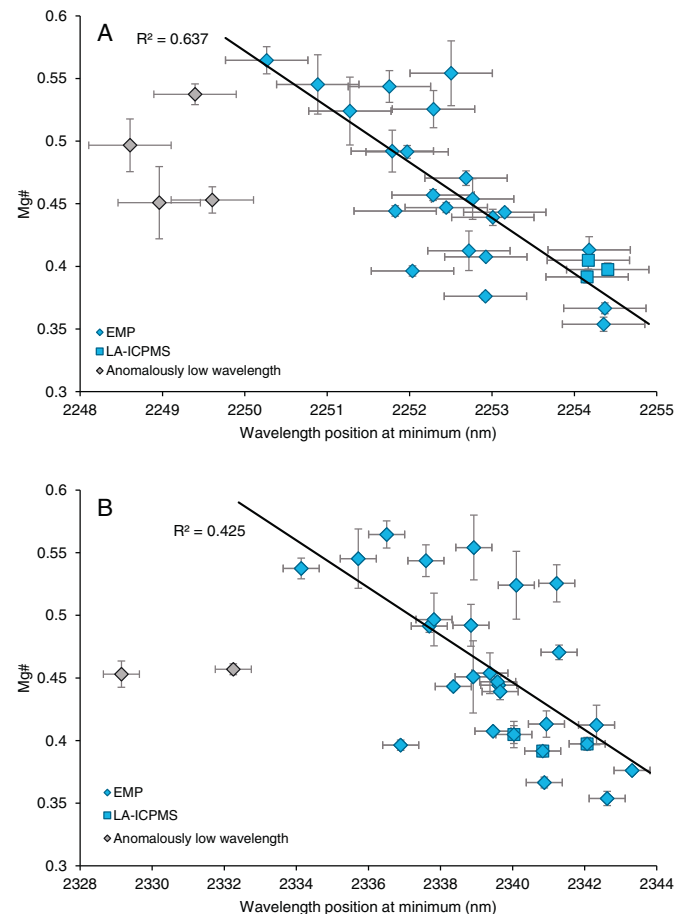


Fig. 10. Chlorite Mg# plotted against the wavelength position at absorption feature minimum for: (A) the 2250 nm absorption; and (B) the 2340 nm absorption. Both features show a reasonably strong negative correlation. Outliers are present at lower wavelengths (shown in grey). Linear regression lines are shown (excluding outliers). Vertical error bars are 1 σ standard error (propagated through the ratio calculation). Horizontal error bars are ± 0.5 nm representing the measurement precision of the spectrometer.

4.4.2. 2250 and 2340 absorption depths

The depths of the 2250 nm and 2340 nm absorptions show similar patterns, deepening systematically away from the porphyry centre (Fig. 18). The vector to mineralisation remains strong, albeit less clear than in the case of wavelength positions. The Sekongkang prospect is not picked out by feature depth variation which is interesting as a potential discriminator between well-mineralised and poorly mineralised systems. Unlike the wavelength positions, absorption depths continually deepen away from the centre (Fig. 19), although values are unusually elevated at around 1 km to 1.5 km.

4.4.3. Major element chemistry

The chlorite Mg/Fe substitution, as reflected by the Mg#, is likely to be the principal control on absorption position and possibly depth. This also shows systematic, but slightly more complicated, changes from the centre outwards (Fig. 20). Chlorite, within approximately 1 km of the centre, is enriched in Mg and then shows a rapid decrease in Mg:Fe ratio to around 1.5 km; beyond this, the relative content of Mg increases progressively to the limit of sampling at about 4.5 km. Samples at distances less than 500 m from the centre (which correspond to tonalite and carbonate-hosted chlorite) are anomalous, as previously identified in chlorite trace element chemistry (Wilkinson et al., 2015).

The Al:Si ratio in chlorite shows a fairly strong inverse correlation with distance, particularly at distances beyond 3 km from the centre (Fig. 21). However, this is not reflected in any obvious spatial variation

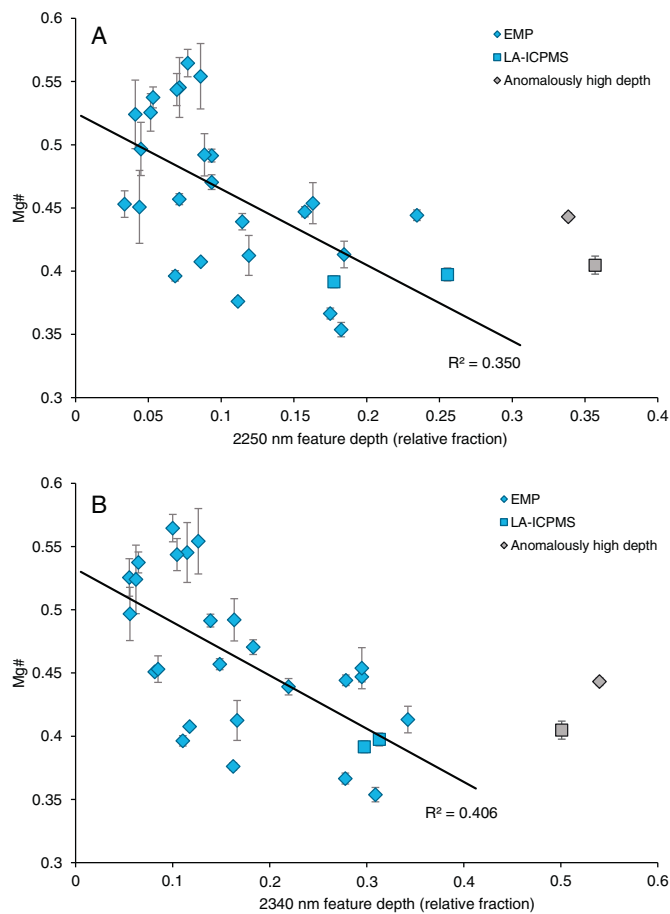


Fig. 11. Chlorite Mg# plotted against the relative depth of absorption features for: (A) the 2250 nm absorption; and (B) the 2340 nm absorption. Both features show a negative correlation. Depths greater than ~0.34 are thought to be outliers possibly due to epidote in the sample (shown in grey). Vertical error bars are 1 σ standard error (propagated through the ratio calculation). Horizontal error bars calculated from the signal-to-noise ratio of the spectrometer are not shown as they were determined to be negligible ($\pm 0.025\%$).

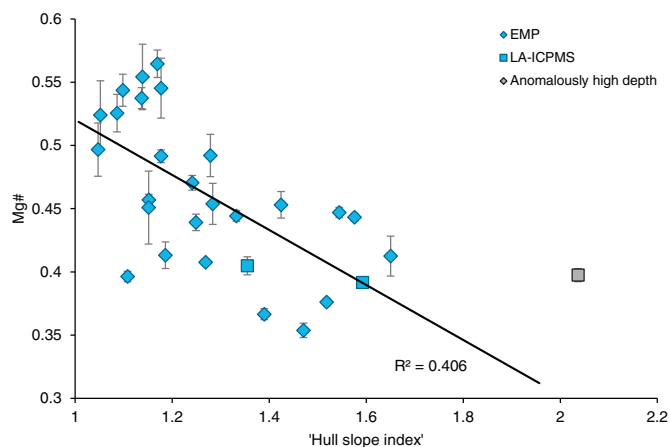


Fig. 12. Chlorite Mg# plotted against the 'hull slope index' (reflectance at 1850 nm/reflectance at 1440 nm) which corresponds to the slope of the hull. Greater values represent steeper slopes. Data points at the highest end appear anomalous (shown in grey) and may reflect the presence of other Fe-bearing minerals in the samples. Vertical error bars are 1 σ standard error (propagated through the ratio calculation). Horizontal error bars calculated from the signal-to-noise ratio of the spectrometer and error propagation are not shown as they were determined to be negligible ($\pm 0.06\%$ and lower).

in the position of the 1400 nm feature (which is thought to be correlated with Al/[Al + Si]). This may be due, in part, to that fact that no samples beyond 3 km displayed chlorite-dominated spectra.

5. Discussion

The results from this study support the effectiveness of reflectance spectroscopy in discriminating alteration zones (e.g. Sun et al., 2001; Jones et al., 2005; Zadeh et al., 2014). In detail, the minerals identified in spectra are generally consistent with the documented alteration mineralogy around Batu Hijau (Clode et al., 1999; Garwin, 2002). The dominance of clay minerals in the central biotite zone likely represents a sensitive response to the late-stage sericite/paragonite and intermediate argillic alteration overprints (Fig. 2; Garwin, 2002). It is unsurprising that biotite was not identified in the spectra given its remarkably low reflectance (Cudahy et al., 2001) especially when occurring alongside highly reflective smectites. However, vermiculite, which can form from hydrothermal alteration of biotite, was identified. The presence of chlorite in the biotite zone, and its dominance (alongside epidote) in the propylitic zone are consistent with expected propylitic alteration assemblages (e.g. Cooke et al., 2014a). Actinolite, where present, generally occurs in proportions too low to be detected. Zeolite minerals identified in distal samples have been previously noted and attributed to a final, low temperature, alteration stage (Clode et al., 1999).

Geochemical variation in chlorite has previously been recognised as an effective vector to mineralisation in the Batu Hijau system (Wilkinson et al., 2015). The major element geochemistry derived from electron microprobe analysis unsurprisingly matches that previously reported by LA-ICP-MS (Wilkinson et al., 2015) and shows that Mg# and Al:Si ratios in chlorite vary spatially with respect to the orebody. The lack of correlation between chlorite and whole-rock Mg# suggests that bulk rock composition is not a primary control of chlorite chemistry. An increase in chlorite Fe content away from the porphyry centre to a distance of ~1.5 km has been proposed to occur as a result of the outward advection and cooling of hypersaline brines enriched in Fe (Wilkinson et al., 2015). Al:Si ratios in chlorite vary as a result of substitution in the tetrahedral site (Deer et al., 2009) and are linked to fluid temperature (Cathelineau, 1988). Ca concentrations may be controlled by this reaction, and other major 2^+ ions are also likely to be involved including Mg^{2+} and Fe^{2+} , as well as trace elements such as Sr^{2+} .

These mineral chemical patterns are reflected in SWIR spectral features, especially those centred around 2250 nm and 2340 nm. It is well established that the chlorite Mg# influences the wavelength positions of these features, with more Fe-rich chlorites causing shifts to higher wavelengths (Yang and Huntington, 1996; Herrmann et al., 2001; Jones et al., 2005; Bishop et al., 2008), and this study confirms this relationship. Features in this region are all attributed to overtones of metal-OH bond stretching and bending (Hunt, 1977) which will be affected by the mass and/or ionic radius of the cations involved.

The apparent increase in absorption depths with decreasing Mg# in chlorite is not documented in any other study and may represent a new finding, but caution should be exercised with this interpretation. It is important to consider whether or not the Mg# is linked to increases in absorption depths, or if both factors are independently controlled by another variable that shows the same spatial pattern. If Mg# does directly control the absorption depth, this is postulated to be a result of the higher mass Fe cations having a stronger effect on the metal-OH bond stretches and vibrations.

An alternative explanation is that an increase in the abundance of chlorite in a sample causes an increase in the depth of its unique absorption features. This is because in any mixed (polymineralic) spectrum the prominence of a feature attributable to one mineral directly

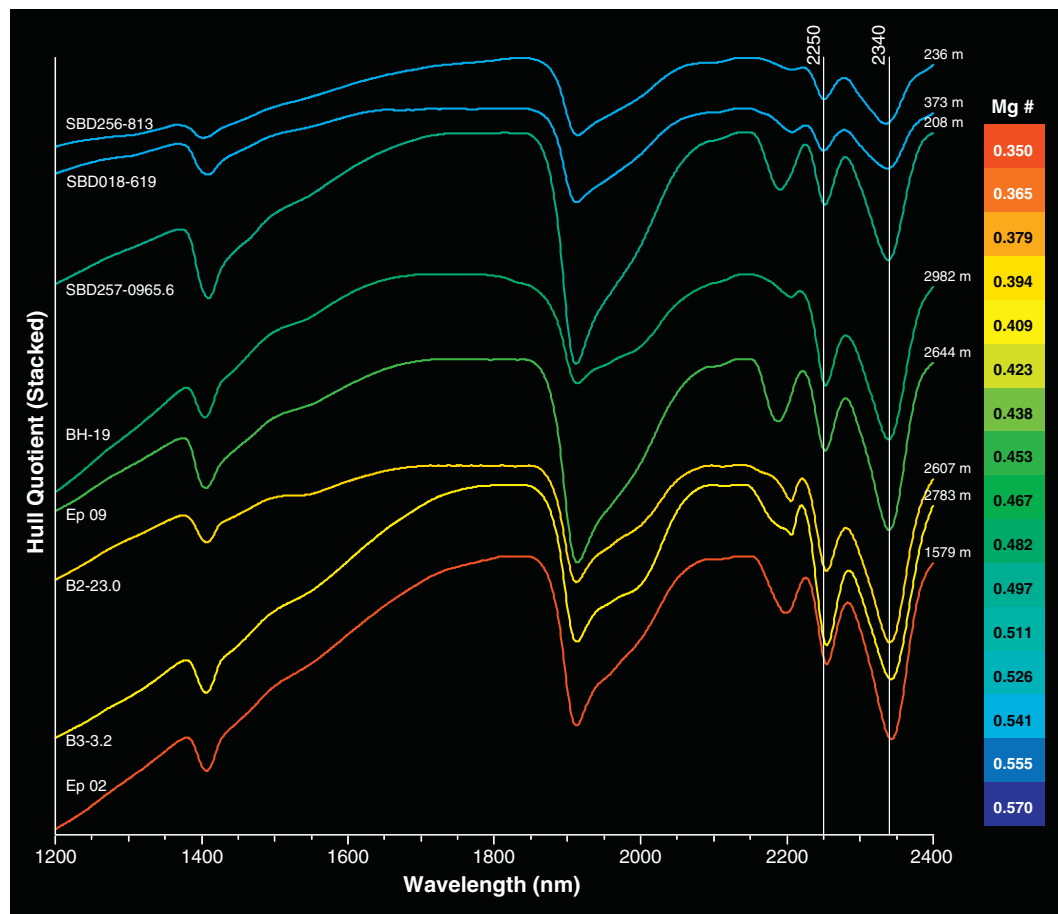


Fig. 13. Chlorite-dominated (hull-quotient corrected) spectra selected to illustrate changes in features. Spectra are stacked in order of the 2340 nm position and coloured according to Mg#. Distances from the sample site to the centre of the orebody are also labelled. Both the 2250 nm and 2340 nm features show a shift to higher wavelengths with decreasing Mg#. Feature depths also increase with increasing Fe content. A steepening of the hull between ~1400 nm and ~1900 nm is also observed as Fe content increases. (For interpretation of the references to colour in this figure legend, the reader is referred to the web version of this article.)

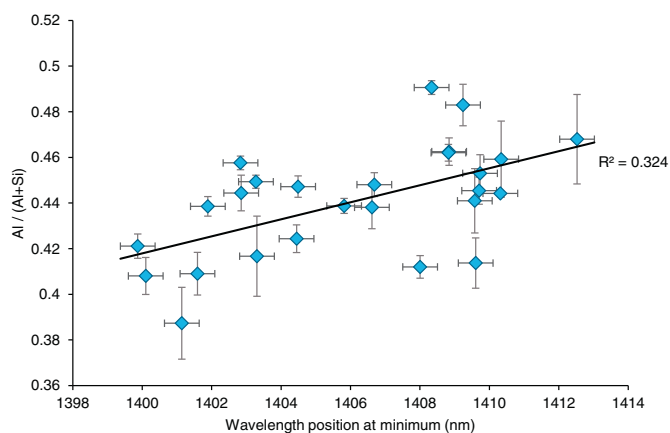


Fig. 14. Chlorite Al/(Al + Si) derived from EMP data plotted against the wavelength at the 1400 nm absorption feature minimum. A reasonably strong positive correlation is seen. Vertical error bars are 1σ standard error. Horizontal error bars are ± 0.5 nm representing the measurement precision of the spectrometer.

depends on its proportion in the sample (Thompson et al., 1999; Herrmann et al., 2001). However, this explanation would contradict studies that have found chlorite abundance to decrease away from porphyry centres (Norman et al., 1991) rather than increase. In the Batu Hijau samples, the proportion of chlorite has not been accurately determined so that this possibly cannot currently be tested.

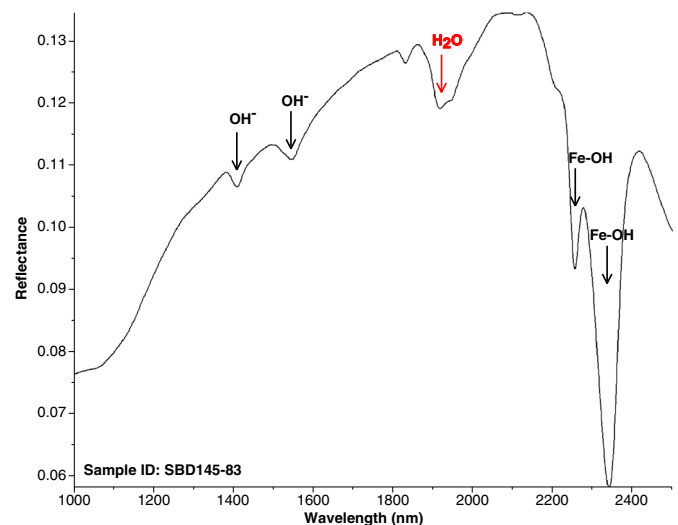


Fig. 15. SWIR spectrum of a sample predominantly made up of epidote. Diagnostic features include the deep Fe-OH absorption features at ~2250 and ~2340 nm, and the OH⁻ absorption at 1550 nm.

The effect of mixed mineral assemblages on the SWIR spectra of rocks is perhaps the biggest problem encountered in this study. Although both spectral analysis techniques employ spectral unmixing at

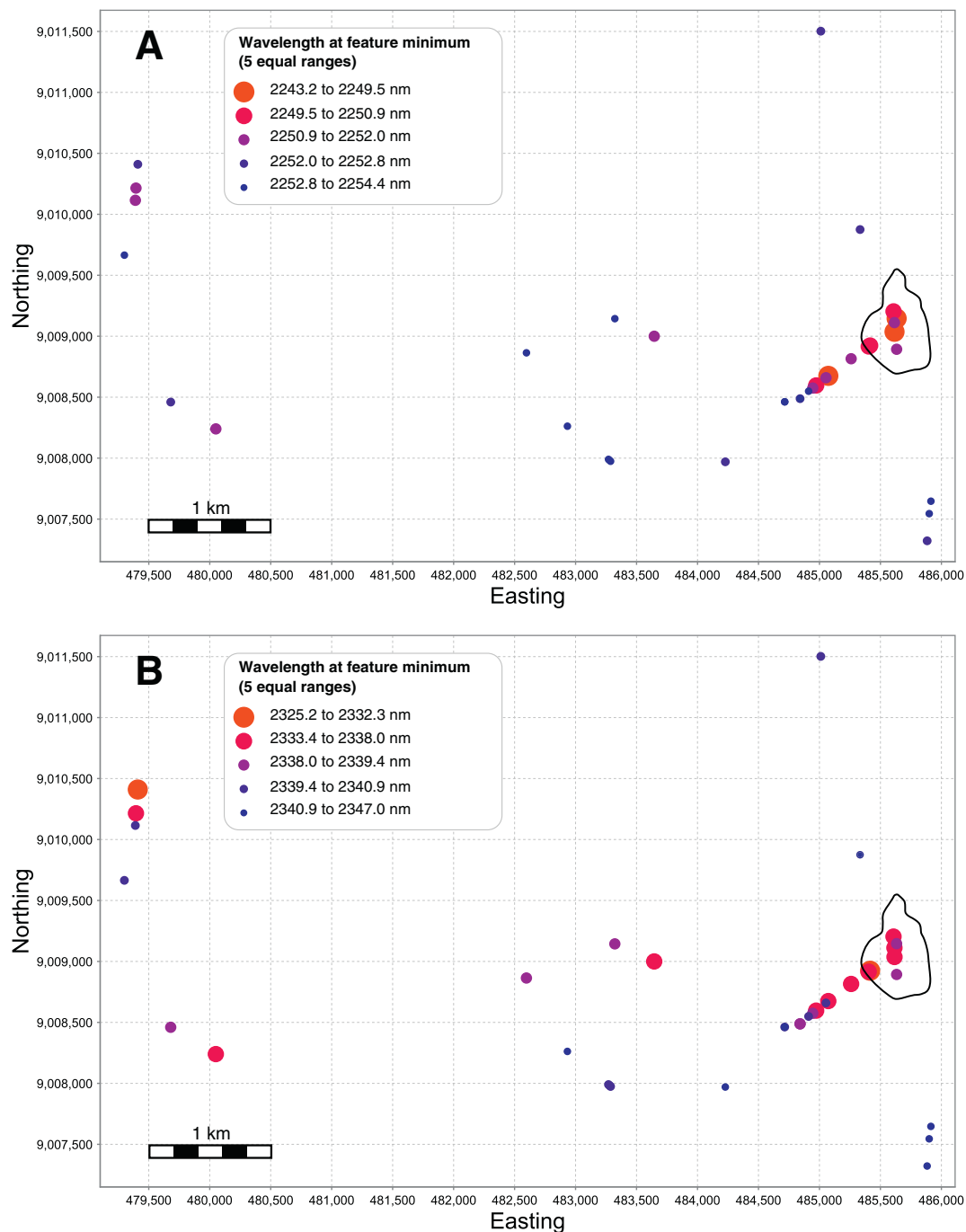


Fig. 16. Spatial variation of (A) the 2250 nm; and (B) the 2340 nm absorption feature positions in chlorite. Larger red circles correspond to shorter wavelengths. A systematic shortening of wavelength position is seen towards the centre of the Batu Hijau deposit along the south-west transect for both absorption features. This is also exhibited more weakly in the west towards the Sekongkang porphyry centre for the 2340 nm absorption feature. The 'strong biotite' alteration zone at Batu Hijau is outlined in black. (For interpretation of the references to colour in this figure legend, the reader is referred to the web version of this article.)

their core, the effectiveness is limited – especially when the number of contributing minerals is high and when minerals have overlapping features. For example, the chlorite-epidote-calcite assemblage, which is common in porphyry systems, will have overlapping features in the region of 2340 nm (Dalton et al., 2004). At Batu Hijau, calcite is relatively rare and so presumably has little effect, however epidote is abundant, especially as the secondary mineral in chlorite-dominated spectra. This is likely to affect both of the important chlorite features at 2250 nm and 2340 nm.

In terms of wavelength positions, the narrower range of wavelength

positions that epidote-related absorptions occupy (Table 3) could create a bias in chlorite spectra towards more central positions in such samples. However, the fact that chlorite Mg# correlates with feature positions (Fig. 10) with the same trend as observed in previous studies on epidote-free samples (Yang and Huntington, 1996; Herrmann et al., 2001; Jones et al., 2005; Bishop et al., 2008) indicates that any epidote interference is limited. In terms of depth, the presence of epidote should deepen the 2340 nm absorption feature, which might explain the anomalously high absorption depth values in the plots demonstrating correlations between absorption depth and chemistry (Fig. 11). With

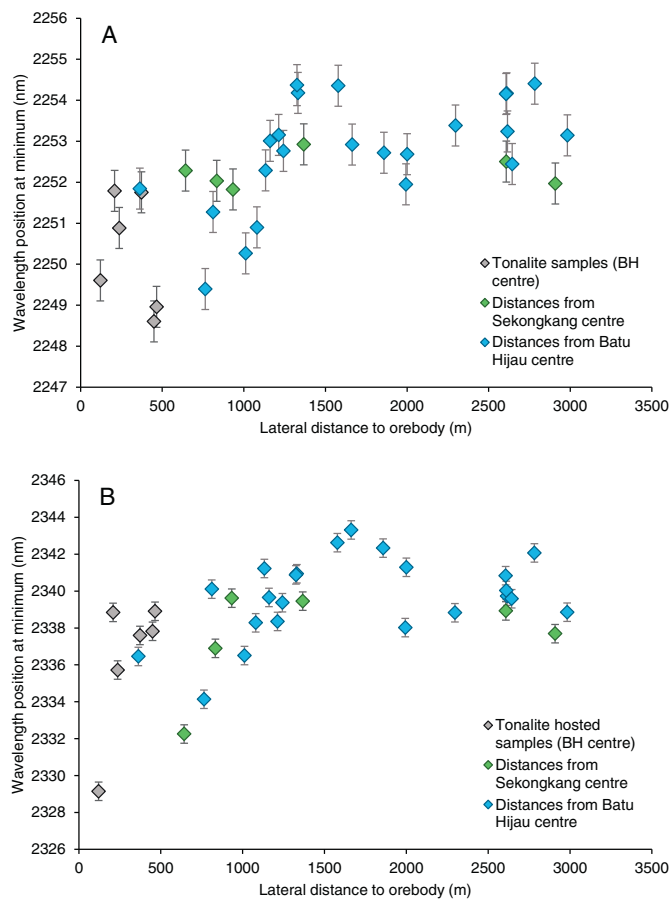


Fig. 17. Wavelength position at the minimum for (A) the 2250 nm; and (B) the 2340 nm absorption features in chlorite plotted against lateral distance to the nearest mineralised centre. Systematic increases are seen outwards to a distance of around 1.6 km with wavelengths decreasing slightly beyond this. Green points indicate samples with distances measured away from the Sekongkang centre rather than Batu Hijau. Grey points correspond to extremely proximal, mineralisation-hosting tonalite samples that are not strictly part of the propylitic halo and may represent a late overprint (see [Wilkinson et al., 2015](#)). Vertical error bars are ± 0.5 nm reflecting the measurement precision of the spectrometer. Horizontal error bars are smaller than the symbol size (uncertainty in sample position is less than 10 m from GPS and the distance to ore estimate is thought to be accurate to within ~ 25 m). (For interpretation of the references to colour in this figure legend, the reader is referred to the web version of this article.)

this considered, the absorption feature at 2250 nm is likely to be a better indicator of chlorite composition than that at 2340 nm. This point is also made in [Herrmann et al. \(2001\)](#) because the secondary Al-OH feature in white mica also overlaps the chlorite feature at 2340 nm. However, use of the 2250 nm feature may be limited in some deposits because it has been shown to completely disappear where there is pervasive weathering ([Suryantini, 2003](#)).

Two other spectral features were shown to vary with chlorite chemistry – the slope of the hull between 1400 nm and 1900 nm, and the position of the 1400 nm absorption feature. The increase in hull slope in more Fe-rich chlorite has been recognised previously ([Thompson et al., 1999](#)) and is attributable to the strong, broad absorption caused by electronic (charge transfer) effects in Fe^{2+} in the VNIR ([Hunt, 1977](#); [Clark et al., 1990](#)). However, this feature occurs in many Fe-bearing minerals and so may just reflect an abundance of these in the rock, rather than a specific response to chlorite, thus explaining the lack of any strong systematic spatial variation. The 1400 nm wavelength position appears to relate to the Al:Si ratio in chlorite. Shifts in this absorption have been previously observed in chlorite ([King and Clark, 1989](#)) and are likely due to modification of the O–H vibration

frequencies as a result of the Tschermark substitution ([Duke, 1994](#)). Unlike the hull slope, this feature appears to offer considerable promise for use in exploration using field-portable or core-shed-based SWIR spectrometers. However, both features are inapplicable to satellite remote sensing due to strong atmospheric scattering effects at these wavelengths ([Duke, 1994](#)).

This study has been unable to conclude anything about potential mineral chemical controls on spectral variations of epidote due to a distinct lack of overlapping data: of the 16 samples that could be classified as epidote-dominated, only five had accompanying geochemical data. This is unfortunate because epidote has shown promise as a vectoring tool in porphyry deposits ([Cooke et al., 2014b](#)) and spectral variation across the epidote-clinzoisite solid-series is certainly recognisable ([Roache et al., 2011](#)). This is an area where future study would be useful.

6. Potential application to satellite remote sensing

The results from this study indicate that porphyry deposits could be targeted by using the absorption features at 2250 nm and 2340 nm which differ between Mg-rich chlorite that can be dominant in the inner propylitic zone ([Wilkinson et al., 2015](#)) and Fe-rich chlorite that can predominate further out, or which may be developed above buried porphyry systems ([Halley et al., 2015](#)). The precise wavelength positions can only be exploited, at present, using field spectrometers or hyperspectral sensors that are capable of collecting high-resolution spectra. It should therefore be possible to target porphyry deposits using hyperspectral imaging, and previous work has demonstrated the discrimination of Fe-chlorite from Mg-chlorite in hyperspectral data ([Cudahy et al., 2001](#)). However, the small wavelength shifts documented here are currently impossible to target using the broad bandwidths (0.02–0.2 μm) typical of satellite remote sensing.

Fortunately, the relative change in absorption feature depth is potentially recognisable using broad-band multispectral imagery collected by the ASTER (Advanced Spaceborne Thermal Emission Radiometer) satellite sensor. ASTER bands 7 and 8 measure surface reflectance in the ranges of 2235–2285 nm and 2295–2365 nm which individually span both absorption features of interest. Deeper absorption features should produce a darker (lower reflectance) response and ASTER band ratio images could perhaps be used to enhance these features.

7. Conclusions

SWIR reflectance spectroscopy is shown to be a powerful tool for characterising propylitic alteration associated with porphyry deposits. The collection of high resolution spectra using handheld spectrometers such as the TerraSpec 4, combined with matching algorithms such as those used by TSG and Halo, allows quick identification of spectrally-active minerals, even in the case of low-reflectance propylitic “green-rocks”. From the spectra, chlorite and epidote were found to be the most abundant SWIR-active minerals in rocks from Batu Hijau, and are in greatest abundance in the more proximal propylitic zone. Spectral signatures from the biotite zone commonly indicate the presence of smectites and other phyllosilicates attributable to later stage, intermediate argillic and sericitic overprinting.

Chlorite chemistry can be utilised as a powerful vector to ore ([Wilkinson et al., 2015](#)) and this appears to translate to features in the SWIR spectra of chlorite-dominated samples. Chlorite from Batu Hijau varies significantly in terms of Mg#, which is likely the main cause of shifts in the wavelength position of absorption features at around 2250 nm and 2340 nm, and possibly the cause of depth variation in these features. The positions and depths of both features act as good vectors to mineralisation: wavelength positions shift from 2254 to 2249 nm and from 2343 to 2332 nm, and absorption depths decrease from around 35% to 5% respectively, moving from ~ 1.6 km to 500 m away from the orebody. This correlates with a general increase in the

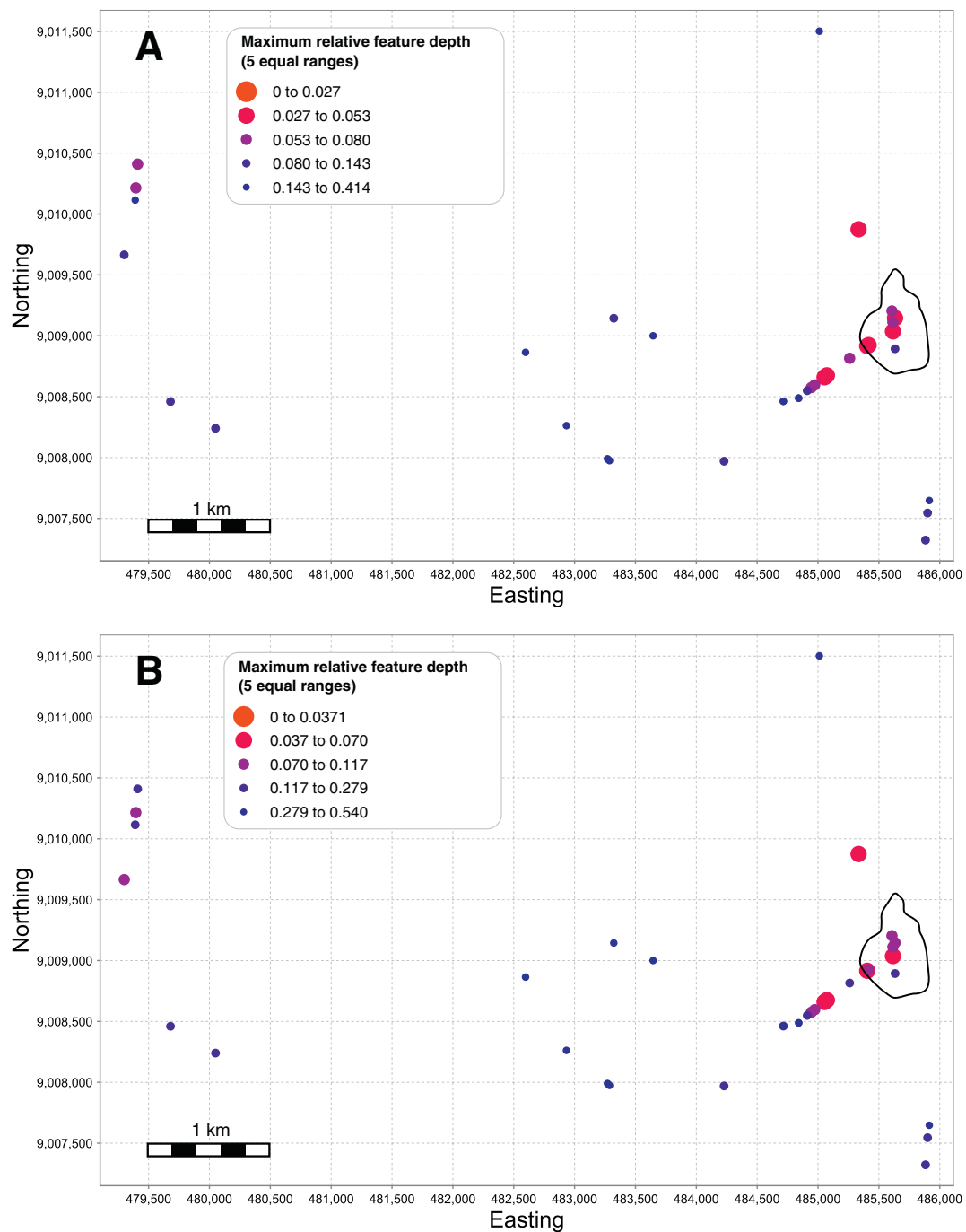


Fig. 18. Spatial variation of (A) the 2250 nm; and (B) the 2340 nm absorption feature depths in chlorite. Larger red circles correspond to shallower absorption features. A fairly systematic decrease is seen towards the centre of Batu Hijau along the south-west transect for both absorption features. No clear trend is observed towards the Sekongkang prospect. The 'strong biotite' alteration zone at Batu Hijau is outlined in black. (For interpretation of the references to colour in this figure legend, the reader is referred to the web version of this article.)

Mg# of chlorite from about 1.6 km towards the fringes of mineralisation. Absorption feature depth variations in particular seem to be a new finding and one potentially more applicable to remote sensing than the well-established position shifts because absorption depth changes can potentially be recognised by satellite remote sensing. The exact cause of changes in absorption depth is not entirely clear, but the fact that this can act as a vector to mineralisation is significant nonetheless, especially if these observations can be recognised in other porphyry systems.

The degree to which these findings apply to other porphyry deposits is still unclear. Furthermore, there is limited information at present to suggest that the variations in alteration mineral geochemistry are specific to fertile (well-mineralised) systems rather than weakly mineralised or barren ones. However, we do note that the 2250 nm peak position and both 2340 nm and 2250 nm absorption feature depths do not appear to highlight the weakly mineralised Sekongkang prospect in the Batu Hijau district. Future work could include investigating chlorite spectral variation in other, variably mineralised, porphyry systems, and

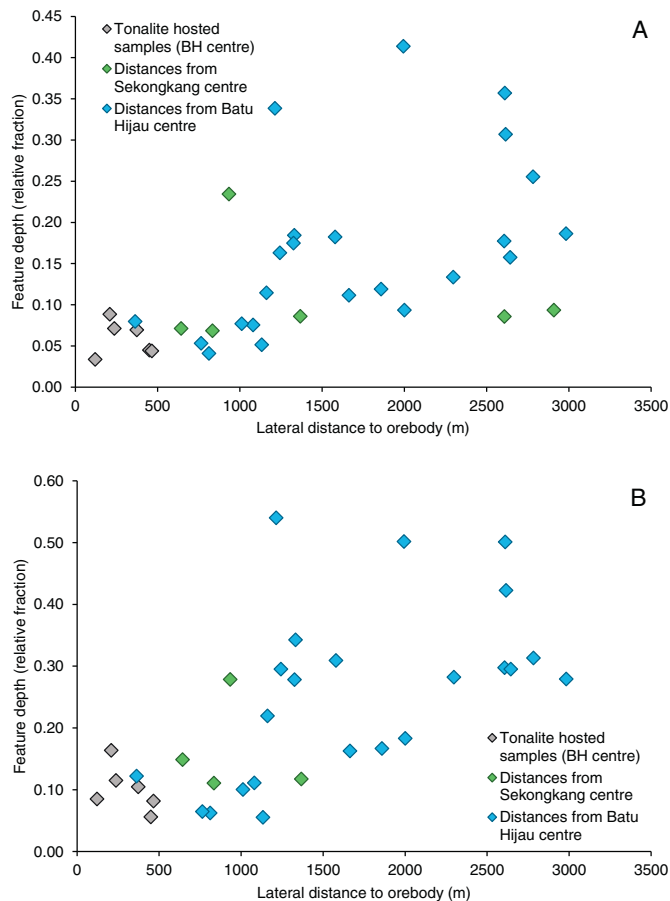


Fig. 19. Relative depths of (A) the 2250 nm; and (B) the 2340 nm absorption features in chlorite plotted against lateral distance to the nearest mineralised centre. A general deepening is observed moving away from the Batu Hijau centre, with slightly elevated values at around 1.3 km to 1.6 km. Note that the same trend is not observed for the Sekongkang prospect, indicating possible utility as a discrimination tool.

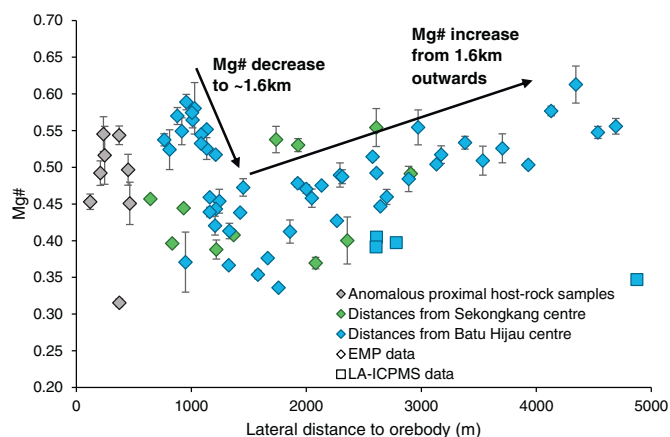


Fig. 20. Chlorite Mg# plotted against lateral distance to the nearest mineralised centre. The data show a sharp decrease in Mg content to a distance of around 1.6 km away from the centre, followed by a steady increase to what may be background levels. No significant relationship is seen in samples measured away from the Sekongkang centre (green). Vertical error bars are 1σ standard error. (For interpretation of the references to colour in this figure legend, the reader is referred to the web version of this article.)

investigating in more detail the effects of epidote. We conclude that SWIR spectroscopy offers significant promise as a practical exploration tool in the “green-rock” environment.

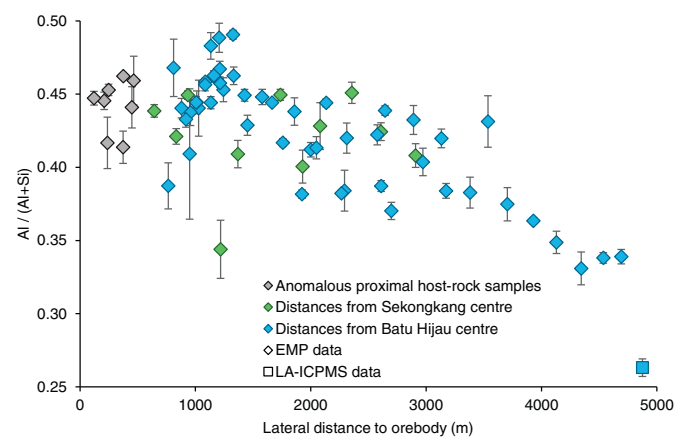


Fig. 21. Al/(Al + Si) content of chlorite plotted against lateral distance to ore. A systematic decrease is observed with distance from Batu Hijau that is not readily apparent in the Sekongkang data. Vertical error bars are 1σ standard error.

Acknowledgements

We thank the AMIRA P765A project team for their previous sampling, research and data collection, and the access and logistical support from Newmont which made the sampling for this project possible. We are extremely grateful to ASD Inc. (PANalytical), in particular Don Campbell and Dan Shiley, for the free loan of the TerraSpec 4 and Halo Mineral Identifier instruments, as well as their technical assistance and advice. We also acknowledge AusSpec for use of *The Spectral Geologist* software. The work was supported by a UROP bursary to Luke Neal, funded by the Department of Earth Science and Engineering at Imperial College London and the London Centre for Ore Deposits and Exploration (LODE), based at the Natural History Museum, London.

References

- AMIRA International Ltd, 2008. Halos in Green Rocks and Lithocaps. www.amira.com.au/web/site.asp?section=projects&page=projectdetails&ProjectLink=2827.
- ASD Inc, 2015. TerraSpec 4 Standard-Res Mineral Analyzer. www.asdi.com/products/terraspec/terraspec-4-standard-res.
- Bishop, J.L., Lane, M.D., Dyar, M.D., Brown, A.J., 2008. Reflectance and emission spectroscopy study of four groups of phyllosilicates: smectites, kaolinite-serpentines, chlorites and micas. *Clay Miner.* 43, 35–54.
- Cathelineau, M., 1988. Cation site occupancy in chlorites and illites as a function of temperature. *Clay Miner.* 23, 471–485.
- Chang, Z., Yang, Z., 2012. Evaluation of inter-instrument variations among short wave-length infrared (SWIR) devices. *Econ. Geol.* 1479–1488.
- Chang, Z., Hedengquist, J.W., White, N.C., Cooke, D.R., Roach, M., Deyell, C.L., Garcia, J., Gemmell, J.B., McKnight, S., Cuisson, A.L., 2011. Exploration tools for linked porphyry and epithermal deposits: example from the Mankayan intrusion-centered Cu-Au district, Luzon, Philippines. *Econ. Geol.* 106, 1365–1398.
- Clark, R.N., King, T.V.V., Klejwa, M., Swayze, G.A., Vergo, N., 1990. High spectral resolution reflectance spectroscopy of minerals. *J. Geophys. Res. Solid Earth* 95, 12653–12680.
- Clode, C., Proffett, J., Mitchell, P., Munajat, I., 1999. Relationships of intrusion, wall-rock alteration and mineralisation in the Batu Hijau copper-gold porphyry deposit. In: Weber, G. (Ed.), 1999 Pacrim Congress, Bali, Indonesia. Australasian Institute of Mining and Metallurgy, Proceedings, vol. 4/99. pp. 485–498.
- Cooke, D.R., Hollings, P., Walshe, J.L., 2005. Giant porphyry deposits: characteristics, distribution, and tectonic controls. *Econ. Geol.* 100, 801–818.
- Cooke, D.R., Hollings, P., Wilkinson, J.J., Tosdal, R.M., 2014a. Geochemistry of porphyry deposits. In: Turekian, H.D., Holland, K.K. (Eds.), *Treatise on Geochemistry*, Second edition. Elsevier, Oxford, pp. 357–381.
- Cooke, D.R., Baker, M., Hollings, P., Sweet, G., Chang, Z., Danyushevsky, L., Gilbert, S., Zhou, T., White, N., Gemmell, B., Inglis, S., 2014b. New advances in detecting the distal geochemical footprints of porphyry systems—epidote mineral chemistry as a tool for vectoring and fertility assessments. In: Kelley, K.D., Golden, H.C. (Eds.), *Building Exploration Capability for the 21st Century*. Society of Economic Geologists, Special Publications, vol. 18. pp. 127–152.
- CSIRO, 2010. TSG Features - Automated Identification. www.thespectralgeologist.com/automated_interps.htm.
- Cudahy, T.J., Okada, K., Yamato, Y., Cornelius, A., Hewson, R., 2001. Mapping the skarn-porphyry-epithermal alteration system at Yerington, Nevada, using VNIR-SWIR-TIR

- remotely sensed data. In: CSIRO Exploration and Mining Report 1121R, CSIRO Exploration and Mining, New South Wales, Australia.
- Dalton, J.B., Bove, D.J., Mladinich, C.S., Rockwell, B.W., 2004. Identification of spectrally similar materials using the USGS Tetracorder algorithm: the calcite-epidote-chlorite problem. *Remote Sens. Environ.* 89, 455–466.
- Deer, W.A., Howie, R.A., Zussman, J., 2009. *Rock-Forming Minerals Vol. 3B, Layered Silicates Excluding Micas and Clay Minerals*, 2nd edition. Geological Society, London.
- Dilles, J.H., 2012. Footprints of porphyry Cu deposits: vectors to the hydrothermal center using mineral mapping and lithogeochemistry. In: Technical Report. Oregon State University.
- Duke, E.F., 1994. Near infrared spectra of muscovite, Tschermak substitution, and metamorphic reaction progress: implications for remote sensing. *Geology* 22, 621–624.
- Emmons, W.H., 1927. Relations of metalliferous lode systems to igneous intrusives. *Trans. Am. Inst. Min. Metall. Eng.* 74, 29–70.
- Franz, G., Liebscher, A., 2004. Physical and chemical properties of the epidote minerals – an introduction. In: Liebscher, A., Franz, G. (Eds.), *Reviews in Mineralogy and Geochemistry*. Mineralogical Society of America, Washington, vol. 56. pp. 1–82.
- Garwin, S.L., 2000. The Setting, Geometry and Timing of Intrusion-Related Hydrothermal Systems in the Vicinity of the Batu Hijau Porphyry Copper-Gold Deposit, Sumbawa, Indonesia. Unpublished PhD thesis. University of Western Australia (484p).
- Garwin, S.L., 2002. The geologic setting of intrusion-related hydrothermal systems near the Batu Hijau porphyry copper-gold deposit, Sumbawa, Indonesia. In: Goldfarb, R.J., Nielsen, R.L. (Eds.), *Integrated Methods for Discovery: Global Exploration in the Twenty-First Century*. Society of Economic Geologists, Special Publications, vol. 9. pp. 333–366.
- Garwin, S., Hall, R., Watanabe, Y., 2005. Tectonic setting, geology, and gold and copper mineralization in Cenozoic magmatic arcs of Southeast Asia and the West Pacific. In: *Economic Geology*, 100th Anniversary Volume, pp. 891–900.
- Halley, S., Dilles, J.H., Tosdal, R.M., 2015. Footprints: hydrothermal alteration and geochemical dispersion around porphyry copper deposits. *Soc. Econ. Geol. Newslett.* 100, 12–17.
- Herrmann, W., Blake, M., Doyle, M., Huston, D., Kamprad, J., Merry, N., Pontual, S., 2001. Short wavelength infrared (SWIR) spectral analysis of hydrothermal alteration zones associated with base metal sulfide deposits at Rosebery and western Tharsis, Tasmania, and highway-reward, Queensland. *Econ. Geol.* 96, 939–955.
- Hunt, G.R., 1977. Spectral signatures of particulate minerals in the visible and near infrared. *Geophysics* 42, 501–513.
- Idrus, A., Kolb, J., Meyer, F.M., 2009. Mineralogy, lithogeochemistry and elemental mass balance of the hydrothermal alteration associated with the gold-rich Batu Hijau porphyry copper deposit, Sumbawa Island, Indonesia. *Resour. Geol.* 59, 215–230.
- John, E.C., 1978. Mineral zones in the Utah copper orebody. *Econ. Geol.* 73, 1250–1259.
- Jones, S., Herrmann, W., Gemmell, J.B., 2005. Short wavelength infrared spectral characteristics of the HW horizon: implications for exploration in the Myra falls volcanic-hosted massive sulfide camp, Vancouver Island, British Columbia, Canada. *Econ. Geol.* 100, 273–294.
- King, T.V.V., Clark, R.N., 1989. Spectral characteristics of chlorites and Mg-serpentine using high-resolution reflectance spectroscopy. *J. Geophys. Res.* 94.
- Liebscher, A., 2004. Spectroscopy of epidote minerals. In: Liebscher, A., Franz, G. (Eds.), *Reviews in Mineralogy and Geochemistry*. Mineralogical Society of America, Washington, vol. 56. pp. 125–170.
- Norman, D.K., Parry, W.T., Bowman, J.R., 1991. Petrology and geochemistry of propylitic alteration at southwest Tintic, Utah. *Econ. Geol.* 86, 13–28.
- Roache, T.J., Walshe, J.L., Huntington, J.F., Quigley, M.A., Yang, K., Bil, B.W., Blake, K.L., Hyvärinen, T., 2011. Epidote-clinzoisite as a hyperspectral tool in exploration for Archean gold. *Aust. J. Earth Sci.* 58, 813–822.
- Sillitoe, R.H., 2010. Porphyry copper systems. *Econ. Geol.* 105, 3–41.
- Sun, Y., Secombe, P.K., Yang, K., 2001. Application of short-wave infrared spectroscopy to define alteration zones associated with the Elura zinc-lead-silver deposit, NSW, Australia. *J. Geochem. Explor.* 73, 11–26.
- Suryantini, N., 2003. The effect of weathering on short-wave infrared reflectance spectra of hydrothermally altered rock in the footwall of the Kangaroo Caves and Sulphur Springs massive sulfide deposits Western Australia. In: *Implication to Hyperspectral Remote Sensing*. International Institute for Geo-information Science and Earth Observation MSc thesis.
- Thompson, A.J.B., Hauff, P.L., Robitaille, A.J., 1999. Alteration mapping in exploration: application of short-wave infrared (SWIR) spectroscopy. *Soc. Econ. Geol. Newslett.* 39, 16–27.
- Wilkinson, J.J., Chang, Z., Cooke, D.R., Baker, M.J., Wilkinson, C.C., Inglis, S., Chen, H., Gemmell, J.B., 2015. The chlorite proximator: a new tool for detecting porphyry ore deposits. *J. Geochem. Explor.* 152, 10–26.
- Yang, K., Huntington, J.F., 1996. Spectral signatures of hydrothermal alteration in the metasediments at Dead Bullock Soak, Tanami Desert, Northern Territory. In: *Exploration and Mining Report 270R*. CSIRO Exploration and Mining, New South Wales, Australia.
- Zadeh, M.H., Tangestani, M.H., Roldan, F.V., Yusta, I., 2014. Spectral characteristics of minerals in alteration zones associated with porphyry copper deposits in the middle part of Kerman copper belt, SE Iran. *Ore Geol. Rev.* 62, 191–198.